universität wien

MASTERARBEIT / MASTER THESIS

Titel der Masterarbeit / Title of the Master Thesis

„Evaluation of the telescope infrastructure at the University of Vienna for exoplanet transit measurements“

verfasst von / submitted by

Theodor Saalmann, BSc

angestrebter akademischer Grad / in partial fulfilment of the requirements for the degree of

Master of Science (MSc)

Wien, 2022 / Vienna, 2022

Studienkennzahl lt. Studienblatt / degree programme code as it appears on the student record sheet:	UA 066 861
Studienrichtung lt. Studienblatt / degree programme as it appears on the student record sheet:	Masterstudium Astronomie
Betreut von / Supervisor:	Dr. Stefan Meingast

Abstract

Aims: The goal of this thesis is to evaluate the capabilities of the University of Vienna to observe and detect transiting exoplanets. Although in the past there were some successful detections of exoplanet transits by employees and students from the Institute of Astrophysics, there exists no analysis on the exoplanet detection quality. Furthermore, I elaborate on the possibilities for exoplanet follow-up programmes for the Institute of Astrophysics.
Methods: I used two telescopes with their instruments currently installed: the 0.8m Nordkuppel Telescope at the Institute of Astrophysics and the 1.5m Leopold Figl Telescope at the Leopold Figl Observatory for Astrophysics. To provide data that can be compared in a meaningful way, I organised and performed simultaneous observations with both telescopes of the same targets. The two observed exoplanets are HAT-P-36 b and TOI1820 b in the R band. To set up my data analysis tools, I also measured a transit of WASP-11 b with the Nordkuppel Telescope in the V-band beforehand. For data analysis, I performed differential photometry, mainly using the available Python packages and Source Extractor. The observations were evaluated by comparing the light curves and their standard deviation from the two telescopes, as well as the derived astrophysical parameters to the literature.
Results: All observation with the Nordkuppel and Figl telescopes were successful. With the Nordkuppel, the transits of TOI1820 b and HAT-P-36 b were detected at a depth of 0.574 ± 0.002 % and 1.75 ± 0.106 %, respectively. With data from the Figl telescope, I measured depths of 0.303 ± 0.005 % for TOI1820 b and 1.69 ± 0.143 % for HAT-P-36 b. I presented multiple explanations for light curve gradients, like atmospheric extinction and variable stars. An evaluation of the standard deviation of the recorded light curves showed that combining multiple reference stars and using adaptive-sized apertures have a significant impact on the detection quality. In addition, the semi-major axis, the planetary radius, and the inclination were calculated for both exoplanets.
Conclusion: Observing and successfully measuring exoplanet transits is possible with the currently available equipment at the University of Vienna. However, the quality of the results depends on the telescope, detector, target brightness, and available reference stars. In particular, multiple reference stars with a brightness similar to that of the target star are vital to the stability and noise properties of the constructed light curves and the reliability of successful transit observations. Given the larger field of view with its current instrumentation, the Nordkuppel telescope currently outperforms the Figl telescope in measuring exoplanet transits. However, the Figl telescope with its larger aperture reaches fainter target magnitudes, yet is very limited in observable targets because of its small field of view. As a consequence, being part of follow-up programmes for measuring exoplanet transits is currently well within reach with the Nordkuppel and can be significantly enhanced with upgraded instrumentation for the Figl telescope.

Zusammenfassung

Ziele: Die Kernfrage, die sich diese Arbeit stellt, lautet 'Wie gut kann die Universität Wien Exoplaneten detektieren?'. In der Vergangenheit wurden zwar von MitarbeiterInnen und Studierenden des Instituts für Astrophysik Exoplaneten beobachtet, jedoch gibt es keine ausgearbeitete Statistikanalyse über die Detektionsqualität. Ein weiteres Thema dieser Arbeit ist herauszufinden, ob die Instrumente der Universität Wien leistungsfähig genug sind, um an Exoplanetennachbeobachtungsprogrammen teilzunehmen.
Methoden: Für die Beobachtungen wurden die beiden modernsten und größten Teleskope der Universität Wien verwendet: Das 0,8m Nordkuppel Teleskop des Instituts für Astrophysik und das 1,5m Leopld Figl Teleskop des Leopold Figl Observatoriums für Astrophysik. Damit die beiden Teleskope und deren Daten aussagekräftig verglichen werden konnten, wurde eine Parallelbeobachtung mit beiden Teleskopen an dem selben Objekten zur selben Zeit durchgeführt. Die beiden Exoplaneten, die auf diese Weise beobachtet worden sind, heißen HAT-P-36 b und TOI1820 b und wurden im R Band gemessen. Als Test wurde vorher WASP-11 b mit der Nordkuppel im V Band aufgenommen. Für die Datenanalyse wurde differenzielle Photometrie mittels Python und Source Extractor angewandt.
Resultate: Alle Beobachtungen mit dem Nordkuppel und Figl Teleskop wurden erfolgreich durchgeführt und analysiert. Mit der Nordkuppel wurde bei TOI1820 b eine Transittiefe von 0.574±2.1e-3 % gemessen und bei HAT-P-36 1.75±0.106 %. Das Figl Teleskop hat für TOI1820 b eine Tiefe von 0.303±4.6e-3 % und für HAT-P-36 b 1.69±0.143 % gemessen. Weiters wurden die astrophysikalischen Parameter 'große Halbachse', 'Planetenradius' und 'Inklination' für beide Exoplaneten berechnet.
Konklusion: Einen Exoplaneten mit der Instrumentierung der Universität Wien zu beobachten, ist machbar. Das benutzte Teleskop, der Detektor, das Target und die Anzahl der Referenzsterne haben jedoch einen großen Einfluss auf die Messung. Die Datenauswertung hat gezeigt, dass die Helligkeit des Referenzsterns eine ähnliche Helligkeit wie der Targetstern haben sollte und je mehr Referenzsterne desto besser. Da die Nordkuppel mit ihrem großen Bildfeld diesen Anforderungen besser nachkommen kann, ist im Moment die Nordkuppel besser für die Beobachtung von Exoplaneten geeignet. Das Figl Teleskop hat mit seiner größeren Apertur jedoch ein deutlich besseres Rauschpotenzial, und mit ein paar Änderungen der Instrumentierung könnte man ein größeres Bildfeld erzeugen und somit fast alle Vorteile der Nordkuppel erlangen. Bezüglich der Beteiligung an Nachbeobachtungsprogrammen ist dies aktuell mit der Nordkuppel möglich und mit ein paar Aufrüstungsarbeiten mit dem Figl Teleskop deutlich besser realisierbar.

Contents

Chapter 1

Introduction

Space. What is out there? We know much about the world beyond our blue pearl called Earth, but there is still so much more to discover, explain, and explore. Astronomy and Astrophysics are scientific fields dedicated to answering those questions. Those involved are among others cosmologists who try to explain what happened at the beginning of time, stellar physicists who try to understand stars from their birth to death, or astronomers who create maps of our universe. This thesis, however, was written by a planet hunter who searches and detects known or unconfirmed exoplanets. An overview of what exactly exoplanets are, how they are discovered, and why I want to detect them is presented in this first chapter.

1.1 Exoplanets

Simply put, an extra-solar planet (exoplanet) is a planet orbiting a star other than the Sun. However, this definition is lacking, especially when one looks at the already well-developed definition of planets by the International Astronomical Union (IAU) from 2006[1]: A planet is a celestial body that

- is in orbit around the Sun,
- has sufficient mass for its self-gravity to overcome rigid body forces so that it assumes a hydrostatic equilibrium (nearly round) shape, and
- has cleared the neighbourhood around its orbit.

This definition cannot be used for exoplanets, since the bullet point 'is in orbit around the Sun' is contrary to what an extra-solar object is. Therefore, a different way of defining an

[1] https://www.iau.org/static/resolutions/Resolution_GA26-5-6.pdf

exoplanet was needed, and in 2018 the IAU presented the following definition (des Etangs & Lissauer, 2022):

- Objects with true masses below the limiting mass for thermonuclear fusion of deuterium (currently calculated to be 13 Jupiter masses for objects of solar metallicity) that orbit stars, brown dwarfs, or stellar remnants and that have a mass ratio with the central object below the L_4/L_5 instability ($M/M_{central} < 2/(25 + \sqrt{621}) \approx 1/25$) are 'planets', no matter how they formed.
- The minimum mass/size required for an extra-solar object to be considered a planet should be the same as that used in our Solar System, which is a mass sufficient both for self-gravity to overcome rigid body forces and to clear the neighbourhood around the object's orbit.

With these additional conditions, it is now possible to identify an object as an exoplanet. Currently, there are 5154 planets in 3802 different planetary systems (August 29th 2022[2]) and nearly every day new exoplanets are confirmed. There are several online libraries to look up the latest collection on exoplanet data. One of the largest databases is http://exoplanet.eu/, which is also used for this thesis.
The very first exoplanets were confirmed in 1992, orbiting the pulsar PSR B1257+12 and given the names PSR B1257+12 b and PSR B1257+12 c (Wolszczan & Frail, 1992). Planets are named after their host star(s) with the addition of a small letter afterward. Starting with b and moving up the alphabet with increasing distance to their host star. The planets of PSR B1257+12 were detected with the photometric transit method, the same method that I used for this thesis and is explained in Section 3.1. Nevertheless, there are more methods to detect exoplanets:

- Radial Velocity: This exoplanet detection method uses spectral lines from the host star. Stars and their planetary systems revolve around their barycentre, giving rise to small variations in the position of the star itself. This periodic change in radial velocity can be seen in the spectrum. This method is very important for measuring the mass of the exoplanet (Alam et al., 2015).
- Direct imaging: Spatially resolving the planet-star system by using a coronagraph to block the light from the star. This method is only possible with a nearby stellar system (Marois et al., 2008).
- Micro-Lensing: Gravity bends light, and from the right angle a planet can act as a lens, as it increases the detected flux of a star. Free floating planets can be found with this method as well (Penny et al., 2019).

[2] http://exoplanet.eu/catalog/

- Transit timing: Masses interact with each other, and so do multiple exoplanets in the same stellar system. The start of an exoplanet transit can change slightly when another exoplanet is nearby, and this variability can be measured, leading to the detection of new exoplanets (Jontof-Hutter et al., 2016).
- Astrometry: The movement of a star, while orbiting a planet, can be detected by measuring its position with high precision. Periodic variance can be used to detect an exoplanet orbiting the star (Perryman et al., 2014).

To conclude the overview of exoplanets, a list of telescopes and surveys that contributed to the detection of exoplanets is presented below.

Table 1.1: The ground-based projects and space missions of the most successful exoplanet discoveries. Most of them use the transit method, but there are some current and future space missions that use different methods, and these will be discussed in the outlook of this thesis.

Ground-based Projects	**Number of Exoplantes**	**Date**	**Method**
HARPS	130+	2002 - present	Radial Velocity
HAT	109	2001 - present	Transit Method
KELT	26	2005 - 2020	Transit Method
NGTS	20	2015 - present	Transit Method
OGLE	17+	1992 - present	Transit Method / Micro Lensing
TRAPPIST	7	2010 - present	Transit Method
WASP	191	2005 - present	Transit Method
Space Missions			
COROT	34	2006 - 2012	Transit Method
Kepler + K2	3673	2009 - 2018	Transit Method
MOST	1+	2003 - 2019	Transit Method
SWEEPS	16	2006	Transit Method
TESS	82+	2018 - present	Transit Method

Acronyms: High Accuracy Radial Velocity Planet Searcher (HARPS Mayor et al., 2003), HATNet and HAT-South Projects (HAT Bakos et al., 2004), Kilodegree Extremely Little Telescope (KELT Pepper et al., 2007), Next-Generation Transit Survey (NGTS Wheatley et al., 2018), Optical Gravitational Lensing Experiment (OGLE Udalski et al., 1994), Wide Angle Search for Planets (WASP Pollacco et al., 2006), Transiting Planets and Planetesimals Small Telescope (TRAPPIST Jehin et al., 2011), Convection, Rotation and planetary Transits (CoRoT Baglin et al., 2006), Kepler named after Johannes Kepler Howell et al., 2014, Microvariability and Oscillations of Stars (MOST Walker et al., 2003), Sagittarius Window Eclipsing Extrasolar Planet Search (SWEEPS Clarkson et al., 2008), Transiting Exoplanet Survey Satellite (TESS Ricker et al., 2015).

1.2 Follow Up Concept

Confirming the existence of an exoplanet is not as straightforward as it may sound. It is already challenging to correctly execute one of the detection methods, but with only one detection, it is not enough to call the exoplanet confirmed. One of the reasons is the principle that discoveries have to be replicative to be scientifically accepted and validated. considered true. Another reason in this specific case is the possibility of a false positive. It can occur that the measurement was seemingly successful, but the source of the signal comes from something different than an exoplanet. To validate exoplanet detection, follow-up missions can be used to solidify the confirmation. A follow-up observation is a re-observation of an already observed exoplanet, and it is not necessary to use the same telescope or detection method. For instance, getting multiple transits from the same exoplanet delivers great value, but obtaining additional radial velocities can be even more impactful.

Looking into false-positive scenarios, there are multiple astronomical phenomena that can be interpreted as an exoplanet transit. For example, an eclipsing binary (Wilson, 1994) or the variability of a red giant (Groenewegen, 2004) can also cause a change in brightness. It is important to note that there is never a 100 % chance of confirming an exoplanet by observation, but it is possible to validate it. Validating a transiting planet means statistically arguing that the data are much more likely to be explained by a planet than by an astrophysical false positive (Bouma et al., 2020). Exoplanet surveys, like TESS, usually have a low angular resolution because of their large field of view of a single image. This can lead to multiple unresolved stars in a single pixel (Bouma et al., 2020), which is another reason why space telescope observations are often insufficient. Stellar catalogues, such as Gaia (Gaia Collaboration et al., 2016), or speckle photometry (Howell et al., 2011), help identify hidden objects. To eliminate the possibility of binaries and reduce the possibility of background binaries, radial velocity measurements can be applied (Alam et al., 2015). False positive analysis can be highly complex and the Kepler community proposed a guideline on how to approach this topic (Torres et al., 2011; Morton, 2012). The relevant information of this section is that follow-up observations are a fundamental part of exoplanet hunting missions, and any astronomical institution that wants to become or stay relevant on the topic of exoplanets should contribute to some of the missions.

1.3 Goals of this Thesis

Before starting follow-up programmes to contribute to ongoing and upcoming exoplanet missions, technical feasibility must be ensured. For this, some exoplanet observations need to be executed and evaluated. For my thesis, I am presenting an overview of the current capabilities of the telescopes and their instruments of the University of Vienna, together with some suggestions on improvements. There are multiple reasons for using the photometric transit method in this thesis. First, it is one of the more suitable methods, since it is already used for all kinds of variable star analysis. Second, even though the Institute of Astrophysics has two spectroscopes, one features a resolution far too low for exoplanets, and the other one is currently not mounted to an available telescope. As a consequence, radial velocities cannot be measured at the moment. Looking at all those facts, the best way for me to give convincing results and evaluations was to take the telescopes of the Institute of Astrophysics and observe exoplanets with the transit method hands-on.

Chapter 2

Instrumentation

All data were collected using telescopes and instruments from the University of Vienna. Since there are many telescopes of various age and design types available at the Institute of Astrophysics and associated observatories like the Leopold Figl Observatory, I decided to use the two largest and best equipped telescopes for this thesis: the 80 cm Nordkuppel telescope and the 1.5 m Leopold Figl telescope. In the following sections, I describe the parameters of the used telescopes and their instruments.

2.1 Nordkuppel

Being the most up-to-date telescope and the only one with a mirror in the main building of the Institute of Astrophysics, this telescope has already proven to be capable of detecting exoplanet transits in the past. The name Nordkuppel comes from its location, being located in the northern dome of the Institute of Astrophysics. In this thesis, it will sometimes be shortened to NK.

Most of the time the Nordkuppel telescope is used to teach hands-on techniques to students during observation lectures. Nevertheless, there are several scientific publications that include data from this telescope. For example, the work of Handler & Meingast (2011) and Uttenthaler et al. (2016) demonstrated that photometry was viable at the high-end level, and spectroscopy can also be performed reliably. There were also some non-published observations of exoplanets from members of the Institute of Astrophysics, strengthening the argument of using this telescope for follow-up missions. In Tab. 2.1 the technical details of the Nordkuppel telescope and its current CCD camera are listed.

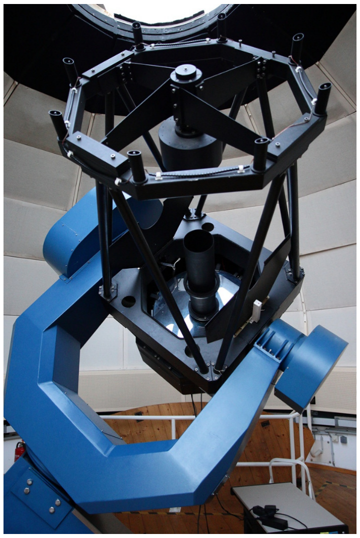

Figure 2.1: The Nordkuppel telescope with opened mirror covers.

Telescope Characteristics	Description
Telescope Model	Cassegrain
Aperture Diameter	80 cm
f-number	f/8.3
Mount	Equatorial
Year of Construction	2002
Instrument Characteristics	**Description**
Camera	CCD ProLine-PL16803
Sensor	KAF-16803
Pixel Count	4096 x 4096
Pixel Size	9 μm
Field of View	19' x 19'
Pixel Scale	0.28" / px
Digital Saturation	2^{16} ADU
Peak Quantum Efficiency	60 % at 550 nm
Filter Options	Bessell BVRI, [OIII], Hα, [SII]

Table 2.1: Overview of the technical parameters of the Nordkuppel telescope and its CCD Camera.

Fig. 2.1 and most of the technical data were taken from a technical article[1] from 2017. The parameters that are especially interesting for this thesis are the aperture of 80 cm and the field of view of 19' x 19', since they differ significantly from the values of the Figl telescope.

2.2 Leopold Figl Observatory

The second telescope that was used for the observations is the main telescope of the Leopold Figl Observatory. This telescope will sometimes be referred to as Figl or FOA (Leopold Figl Observatory for Astrophysics) in this thesis. The occasion for building this facility was the 600-year anniversary of the University of Vienna and was arranged by Lower Austria's governor Leopold Figl, the person the observatory was named after. The ideal location was not easy to find since it should be as dry, dark, and close to the Institute for Astrophysics as possible. In the end, a good compromise was Mitterschöpfel, a hill inside the Wienerwald area located in the west of Vienna.

Two telescopes were constructed, one with an aperture of 1.5 m, making it the largest telescope in Austria to this day, and one with an aperture of 0.6 m. Since the goal of this thesis was to showcase the limits of the University of Vienna photometric capabilities, the larger telescope was chosen. Other reasons were that the 0.6 m telescope needed some

[1] https://astro.univie.ac.at/fileadmin/user_upload/i_astro/Bericht-Nordkuppel.pdf

service repairs at the time and the 1.5 m telescope could be controlled remotely from the Institute of Astrophysics.

The scientific possibilities that the Leopold Figl Observatory offers are far-ranged, which can be seen when looking at some publications and projects. Photometric follow-up observations of asteroids were made by Galiazzo & Zeilinger (2013), and night sky photometry and spectroscopy were performed by Puschnig et al. (2014). For teaching purposes, the light curve of the crab pulsar is detected regularly. A picture of the crab nebula obtained with the Figl telescope is shown in Fig. 2.3. The resulting light curves were a strong argument to perform an in-depth check for the photometric exoplanet detection abilities of the Figl telescope. The 1.5m Figl telescope has multiple operating modes (Cassegrain, Ritchey-Chrétien and Coudé), but for this thesis only the RC focus was used. Table. 2.2 lists the technical details for the Figl telescope and the currently installed imaging system.

Table 2.2: Overview of the technical parameters of the 1.5 m Leopold Figl telescope and the CMOS sensor used. Listed values (e.g. f-number or field of view) refer to the Ritchey-Chrétien operating mode that was used in this thesis.

Telescope Parameter	**Description**
Telescope Model	Ritchey-Chrétien, Cassegrain, Coudé
Aperture Diameter	152 cm
f-number	f/8.3
Mount	Equatorial
Year of Construction	1969
Instrument Parameter	**Description**
Camera Type	CMOS (PICO)
Sensor Type	Andor Zyla 4.2-P
Pixel Count	2048 x 2048
Pixel Size	6.5 μm
Field of View	3.6' diameter
Pixel Scale	0.1" / px
Digital Saturation	2^{16} ADU
Quantum Efficiency	80 % at 550 nm
Filter Options	Bessell VR, Polarisation

Despite both being mirror telescopes, the Nordkuppel telescope and the Figl telescope are different in several aspects. Their biggest difference is the aperture size and the currently installed instruments, which leads to a difference in the field of view: 19' x 19' for the Nordkuppel and 3.6' in diameter for the Figl. These could have a massive impact on exoplanet hunting projects. The consequences will be visualised and discussed in later chapters.

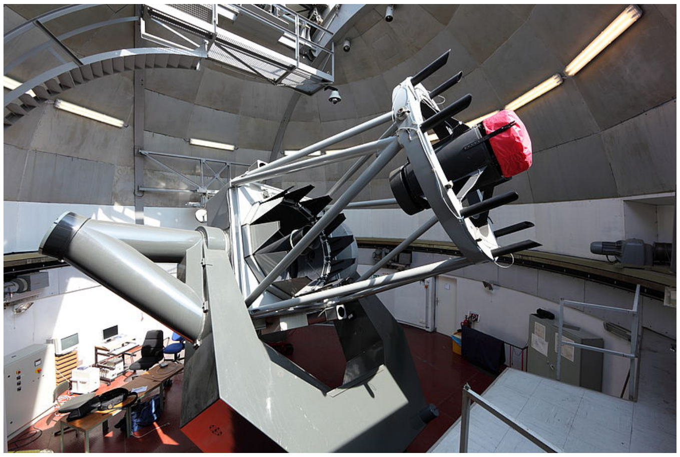

Figure 2.2: The 1.5 m Leopold Figl telescope with an open M1 mirror. The workstation next to the telescope enables remote control of the facility.

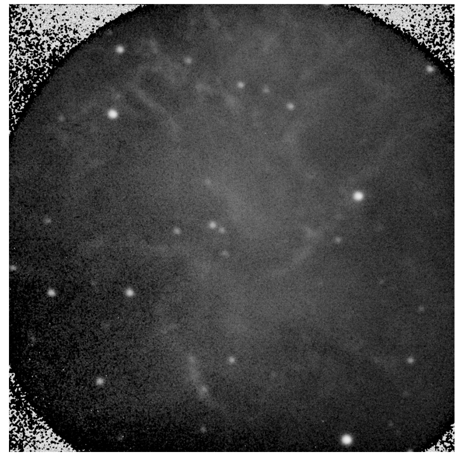

Figure 2.3: Single 30 s image of the Crab Nebula (Messier 1) taken in V-band with the 1.5 m Figl telescope.

Fig. 2.2 and most of the technical data were taken from the official website of the Leopold Figl Observatory for Astrophysics[2].

[2]https://foa.univie.ac.at/

Chapter 3

Methods

In this chapter, theoretical and practical techniques are explained to plan, observe, and analyse an exoplanet transit.

3.1 Transit Method

The exoplanet detection method used in this thesis is called the transit method. The name already suggests that something, in this case, the exoplanet, has to pass in front of an object to be observed. Similarly to a solar eclipse, where the moon transits between the Sun and the observer, an exoplanet moves between a star and the observer during an exoplanet transit. When a planet is in front of a star, it blocks some of its light and makes the star appear dimmer. With the right observation technique, it is possible to detect the change in flux created by this phenomenon. This is usually done with differential photometry (see Sect. 3.2 for a detailed description) in optical or infrared light. The loss of brightness can be as high as a few percent and as low as modern noise limits (Howell et al., 2014), depending on the diameter ratio of the planet to its host star.

Detecting an exoplanet with the transit method has its benefits and disadvantages. There are several astrophysical parameters that can be obtainable with transits, for instance, the semi-major axis or radius of the exoplanet. For some parameters, a different method or additional data are needed. An in-depth overview of the astrophysical parameters of exoplanets is presented in Sect. 3.1.2. Furthermore, without information about the host star, it is impossible to obtain most of the parameters of an exoplanet since many of them are measured in relation to the stellar parameters. The main parameters that astronomers try to measure with the transit method are the orbital period, the semi-major axis, and the radius of the exoplanet. An important parameter that is not measurable by the transit method is the mass of an exoplanet. To obtain the planetary mass, a measurement of the radial velocities of the star-planet system is required for at least one orbit (Alam et al., 2015). One of the main advantages of the transit method is that the required equipment is less complex compared to other methods. Transits can be detected using optical or infrared light, and most earth-bound telescopes are equipped with CMOS or CCD sensors that are sensitive in the optical spectrum.

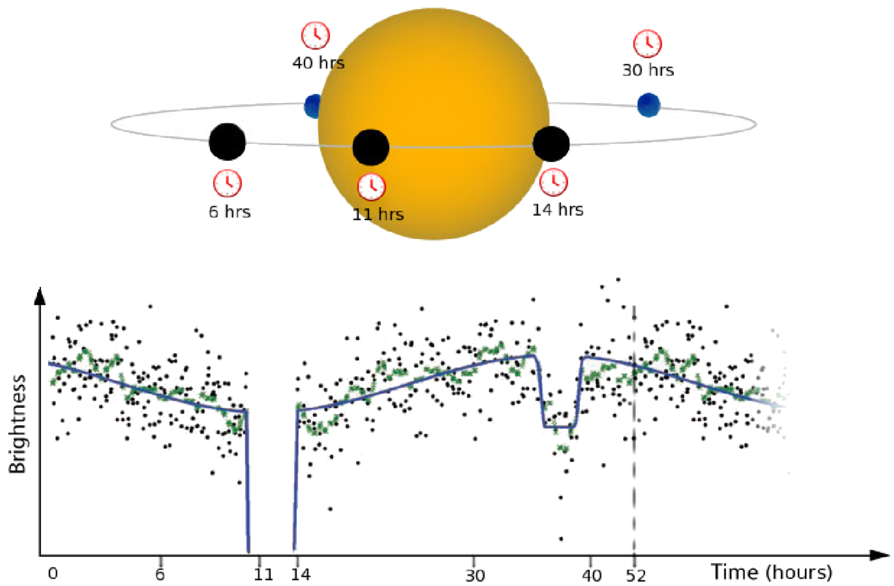

Figure 3.1: This picture from Tinetti et al. (2012) shows the combined measured apparent brightness of the star HAT-P-7 and its planet HAT-P-7b by the Kepler spacecraft (Howell et al., 2014) in dependence of the position of the planet.

3.1.1 Transit light curve

In Fig. 3.1, an ideal light curve of an exoplanet orbit is displayed. On the x-axis, the time from the start of the observation is plotted. On the y-axis, the brightness or flux of the star-planet system is displayed. Each black dot is a single integration, and the green dots are their averages. The blue line is an ideal trend line. The diagram begins with the planet on the far left side of the star. Similarly to a half-moon, the planet is partly illuminated by the host star and therefore increases the detected light during observation. While the exoplanet is continuing its orbit, the illuminated area decreases, and hence the detected flux decreases as well. The brightness drops continuously until the planet begins to cover parts of the star. When the time axis hits about 10 h, the ingress of the transit begins as the planet blocks more and more flux until it is in front of the star and blocks the maximum amount of light with its full projected surface area. Since Fig. 3.1 is a zoom-in of the light curve showing as many features as possible, the main transit dip is cut off (Fig. 3.2 shows the complete primary transit). After about 14 hours the occultation of the star due to the exoplanet comes to an end, and the detected brightness rises abruptly. This is called the egress of a transit. In the illustration, the exoplanet now moves to the right and behind the star. Similarly to a new moon, which gets brighter each night, until it becomes a full moon, the exoplanet becomes seemingly brighter on its way to the far side of the star. At about 36 h, the exoplanet moves behind the star, and the reflected light from its surface can no longer be detected, leading to another, but much smaller, drop in brightness. This is called the secondary transit and has only a small fraction of the depth of a primary transit (Bakos et al., 2010). The secondary transit depth is of the order of only 100 ppm (0.01%), therefore a much smaller effect compared to the noise level of typical light curves that are constructed from ground-based observations.

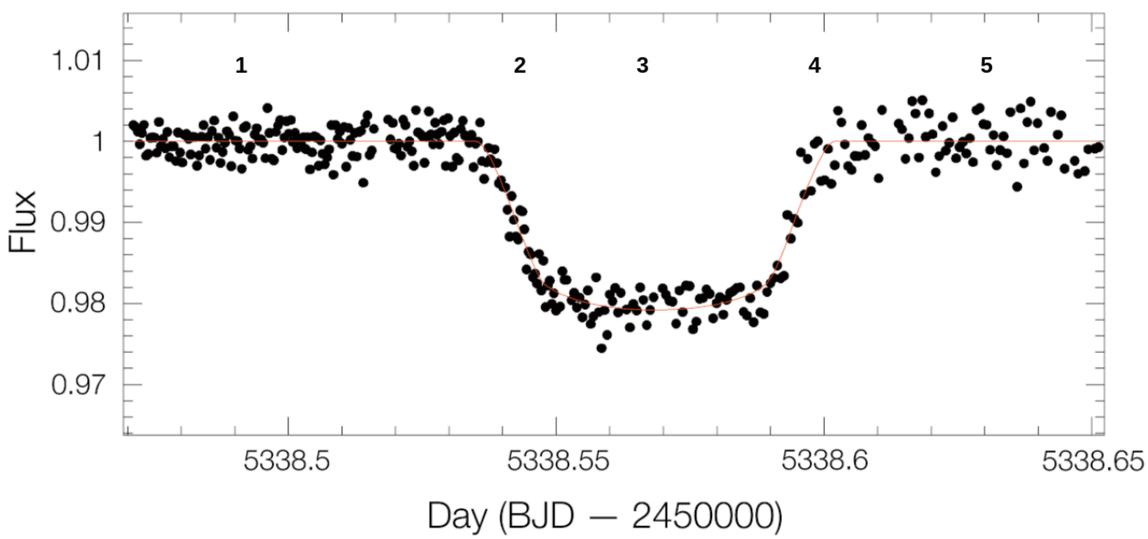

Figure 3.2: This picture from TRAPPIST/M. Gillon/ESO[1] shows the main transit from WASP-19b, detected with the TRAPPIST–South Telescope. Each black dot is a data point of a single image and the red line is an ideal synthetic transit light curve. The labels on top of the light curve refer to different stages of the transit as explained in the main text.

Transit light curves from exoplanets do not necessarily look similar to the example in Fig. 3.2. One of the most common alternative appearances of a transit is the so-called v-shaped transit. This shape, shown in Fig. 3.3, results from an exoplanet transit that only grazes its host star and, therefore, does not occult the host star with the full disk. False positives may occur when dealing with v-shaped light curves because of similarities with light curves from binary stars (Wilson, 1994).

[1] https://www.eso.org/public/switzerland-de/images/eso1023f/

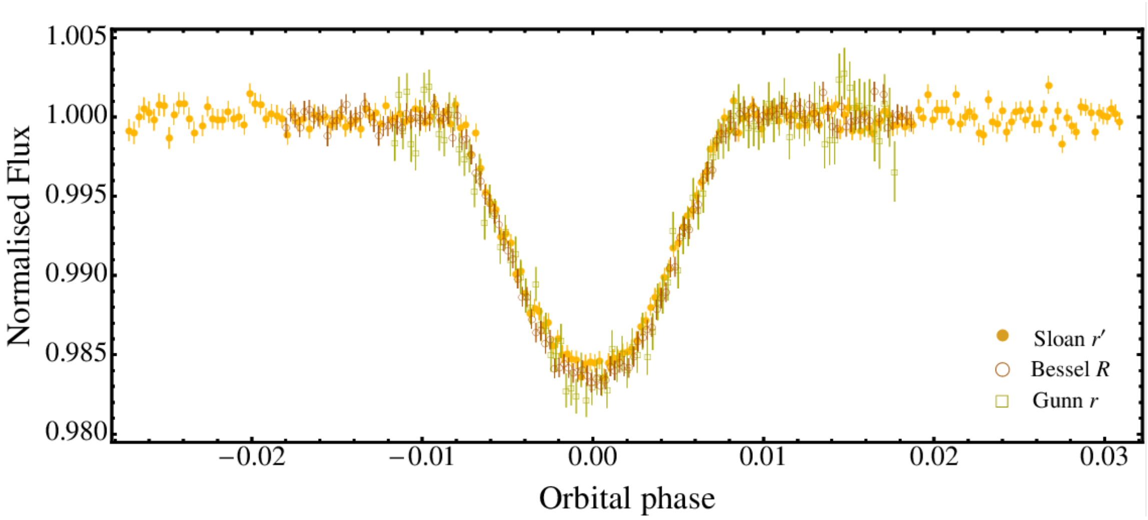

Figure 3.3: This representation of a light curve was adopted from Mancini et al. (2014) and shows the v-shaped transit of one of the planets in the WASP-67 system.

3.1.2 Parameters from the Transit Method

After obtaining one or more light curves from an exoplanet transit, the astrophysical parameters and properties can be extracted from the observation. The orbital period, the semi-major axis, the planetary radius, and the inclination can usually be measured. With a high detection quality, the albedo of an exoplanet and the spots on the surface of a star can also be inferred. In theory, even exomoons should be detectable with the transit method, but until now no exomoons have been discovered. How these parameters can be measured, how they relate to each other, and which characteristics of an exoplanet they can measure are presented with the help of the light curve from the planet HAT-P-7b in Fig. 3.4.

Orbital Period: For this parameter, it is essential to detect the transit of an exoplanet multiple times, ideally at least three times. In Figs. 3.4 A and B, the main transit is clearly visible with an orbital phase duration of about 2.2 days. To obtain the orbital period, the time difference between two transit ingresses, mid-timings, or egresses needs to be calculated.

$$P = t_2 - t_1 \tag{3.1}$$

With P being the orbital period, t_2 the time of the second transit phase (ingress, midterm, or egress) and t_1 the time of the corresponding first transit phase.

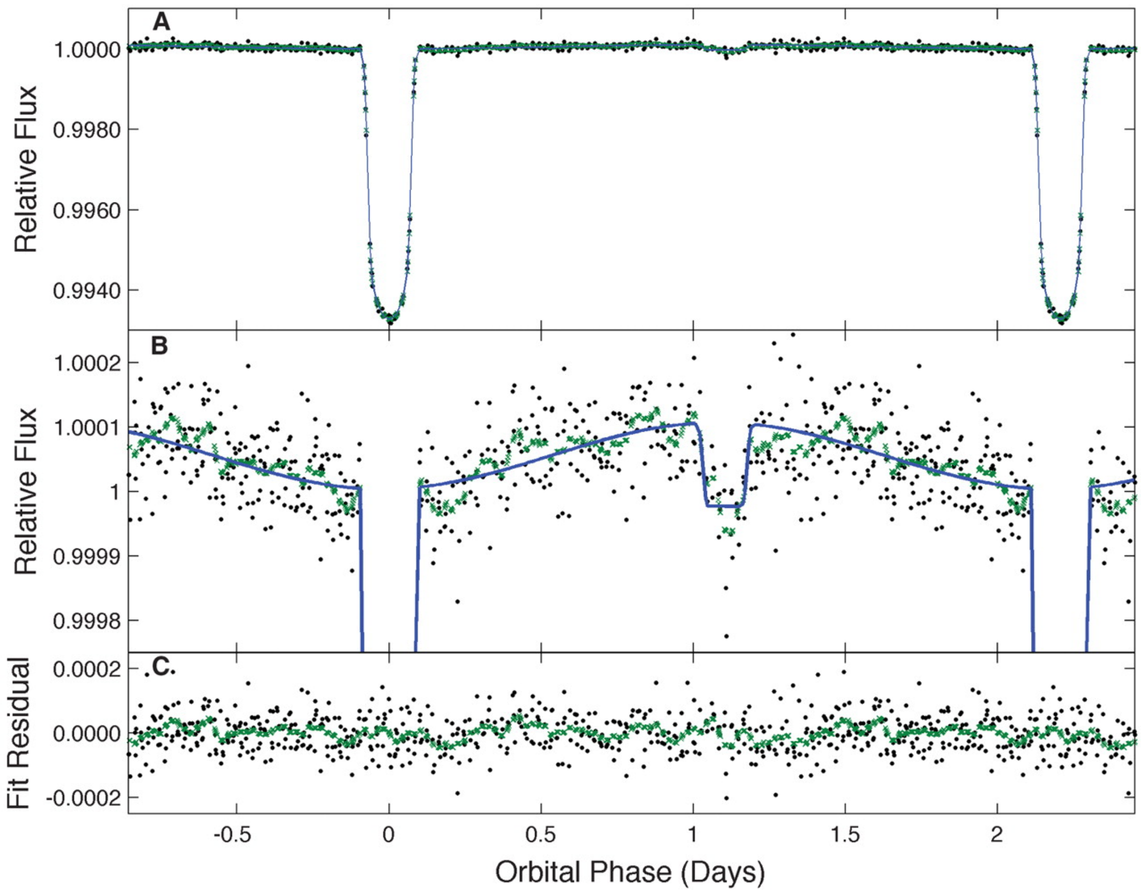

Figure 3.4: This light curve of HAT-P-7b (Borucki et al., 2009) displays excellent signal to noise ratio and multiple transits and allows to derive several astrophysical parameters. In diagram A, the complete light curve is shown with two primary and one secondary transit. The black dots are the individual measurements and the blue line is the trend line. Diagram B is a zoomed-in version of panel A to better show the secondary transit. In panel C, the residuals of the light curve with respect to the fitted trend line are plotted.

Semi Major Axis: After acquiring the period of an exoplanet, its semi-major axis can be calculated. It is preconditioned to know some parameters of the exoplanet host star for the semi-major axis and further calculations of astrophysical parameters of the planet. In the case of the semi-major axis of the exoplanet, the mass of the star is required to use Kepler's third law (Kepler, 1619).

$$P^2 = \left(\frac{4\pi^2}{G(M+m)}\right)a^3 \tag{3.2}$$

With P being the orbital period, G the gravitational constant, M the mass of the host star, m

the mass of the exoplanet (negligible because $m << M$) and a is the semi-major axis. Since the mass of a star is generally not as readily available in the literature as its luminosity, the mass-luminosity relation is frequently used to determine the mass of the star (Kuiper, 1938).

$$\frac{L_S}{L_\odot} = \left(\frac{M_S}{M_\odot}\right)^a \tag{3.3}$$

With L_S being the luminosity of the host star, $L_\odot$ the luminosity of the Sun, M_S the mass of the host star, $M_\odot$ the mass of the Sun and a is an exponential factor, depending on M_S (1 < a < 6 (Salaris & Cassisi, 2005)).

Radius: For deriving the minimum radius of an exoplanet, it is necessary to know the depth of the transit and the radius of the star.

$$\Delta F = \left(\frac{R_P}{R_S}\right)^2 \tag{3.4}$$

With ΔF being the depth of the transit, R_P the radius of the planet, and R_S the radius of the star. This method can only provide the minimum radius of the exoplanet because in the case of a grazing transit, the planet only occults the star with parts of its surface.

Inclination: To determine the inclination of the orbital plane of the exoplanet with respect to the observer, the duration of the complete transit must be known. The specific duration needed is from the beginning of the ingress to the end of the egress. With the help of some geometry and the Pythagoras Theorem, the impact parameter (the sky-projected distance from the centre of the star) and the inclination can be derived via

$$\tau = \frac{P}{\pi} sin^{-1}\left(\frac{\sqrt{(R_s + R_p)^2 - (bR_s)^2}}{a}\right) \tag{3.5}$$

$$b = \frac{a\ cos(i)}{R_s} \tag{3.6}$$

with τ being the duration of the full transit, P the orbital period, R_S the radius of the star, R_P the radius of the planet, b the impact parameter, a the semi-major axis, and i the inclination.

Albedo: Figure 3.4 B shows that the light curve does not appear horizontal between the main and secondary transits. For instance, the rise in luminosity between 0 and 1 day indicates that by moving behind the star, the exoplanet reflects more and more light with each observation. If the exoplanet were a body that reflects no light, the light curve would appear horizontal. Analysing the gradient of the light curve between the transit dips allows to investigate the albedo of the exoplanets (Lendl et al., 2020).

Exomoons: In theory, the detection of an exomoon, the moon of an exoplanet, follows the same pattern as the detection of an exoplanet (Luis et al., 2011). The moon masks part of its host star, and therefore an additional dip in the exoplanet light curve becomes visible, as seen in Fig. 3.5. However, there are two issues. First, the signal-to-noise ratio is even more critical for an exomoon light curve, since moons are smaller than their host planets. Second, for the transit method to work, the exomoon itself needs to have the right inclination. For an exomoon light curve, this has to happen for both the planet and its moon, which makes it statistically less frequent than detecting only an exoplanet.

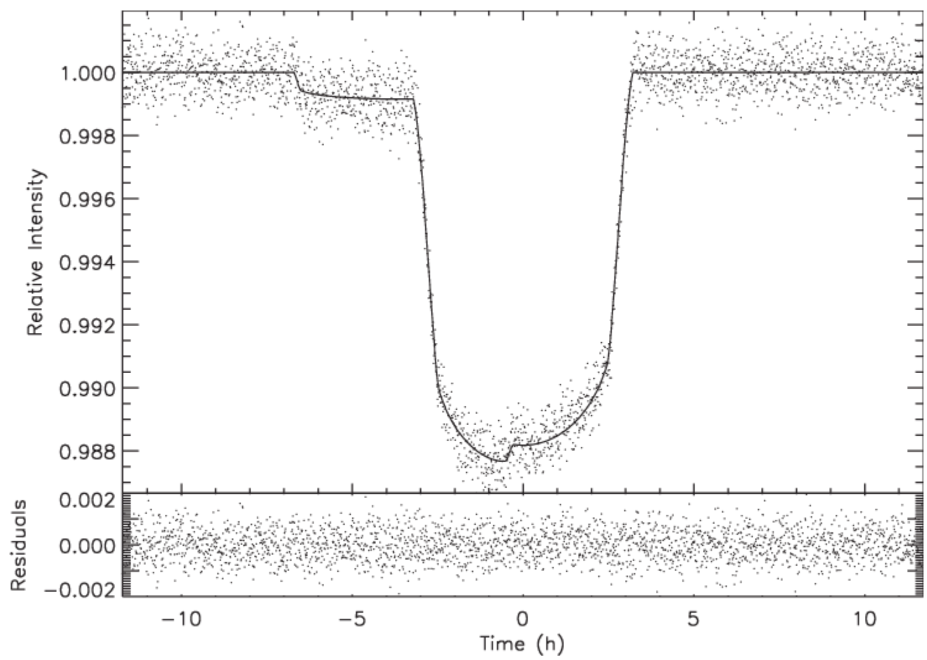

Figure 3.5: A simulated light curve of an exoplanet transit with an exomoon from Luis et al. (2011).

Starspots: Star spots are areas on the surface of a star where magnetic field lines emerge, reducing photon flux and, therefore, cooling and dimming the surrounding surface area. If an exoplanet transits in front of such a spot, it does not block as much light as usual, which can be seen as a temporary brightness increase in the transit light curve. With knowledge of the inclination of the planet, the brightness of the spot, and the timing of the detection, statements about the star spot can be made, and therefore statements about the magnetic activity of the star as well (Agol et al., 2010). In addition, it can happen that star spots are mistaken for exoplanets, since they also decrease the visible brightness of an observed star (Queloz et al., 2001).

However, a specific and critical parameter of exoplanets cannot be obtained by measuring transits: their mass. As a consequence, to obtain a complete spectrum of exoplanet parameters, multiple detection methods have to be used.

3.2 Differential Photometry

A method well suited for analysing exoplanet transits observed from the ground is differential photometry. Photometry is the science of measuring and analysing light at ultraviolet, optical, and infrared wavelengths. In an astronomical context, such measurements are usually made using telescopes with lenses or mirrors equipped with CCD or CMOS detectors. The observed images are stored on a computer and can be analysed with various (astronomical) image-processing software. A typical example of photometry in the context of Astronomy is the measurement of stellar fluxes, done, for instance, by the 2MASS survey (Skrutskie et al., 2006) for nearly the whole sky in the near-infrared, or more recently and in the optical spectrum by the Gaia mission (Gaia Collaboration et al., 2016).

In Astronomy, a popular method of performing photometry is measuring the flux of an object as imaged on the detector. This can be done by measuring the total flux of an object in a fixed-size circular aperture, a method called aperture photometry. Alternatively, cropping, a popular method for space observatories, digitally masks detector areas that will not be used for measurements and instead defines the areas for measurements in advance. In this work, the aperture photometry method was used to extract the flux of point sources for further analysis.

Figure 3.6 displays the aperture photometry setup. Here, the green circle defines the aperture that is used to measure the total flux of the star (and background) in its centre. A little further out, two cyan apertures create a ring, ideally devoid of other sources. This annulus is used to determine the local background value. Specifically, the recorded flux of all individual pixels is averaged, giving the mean background brightness per pixel, calculated as

$$F_{BG}\ [ADU/pixel] = \left(\sum_{i=1}^{n} F_{BGi}\right) / \ n \tag{3.7}$$

with F_{BG} being the mean background flux of one pixel, F_{BGi} the flux of a single pixel, and n the number of pixels in the aperture ring. Equation 3.7 creates a mean, but in this case the calculation of the median can be more robust, since this metric effectively removes outliers and dead pixels. Furthermore, since there can be a brightness gradient on images, due to e.g. scattered light or untight instrument chassis, a more robust approach is to calculate the background value for each star individually. Once the average background brightness is determined, it needs to be subtracted from the flux measured in the central aperture. This can be done by multiplying the background value per pixel by the number of pixels of the aperture used. This background value then needs to be subtracted from the flux inside the main aperture to obtain the background-free stellar flux via

$$F_s\ [ADU] = \left(\sum_{i=1}^{n} F_{si} \right) - F_{BG} \cdot n \tag{3.8}$$

with F_s being the final flux of a star, F_{si} the flux of a single pixel in the star aperture, F_{BG} the mean background flux of one pixel, and n the number of pixels in the central aperture.

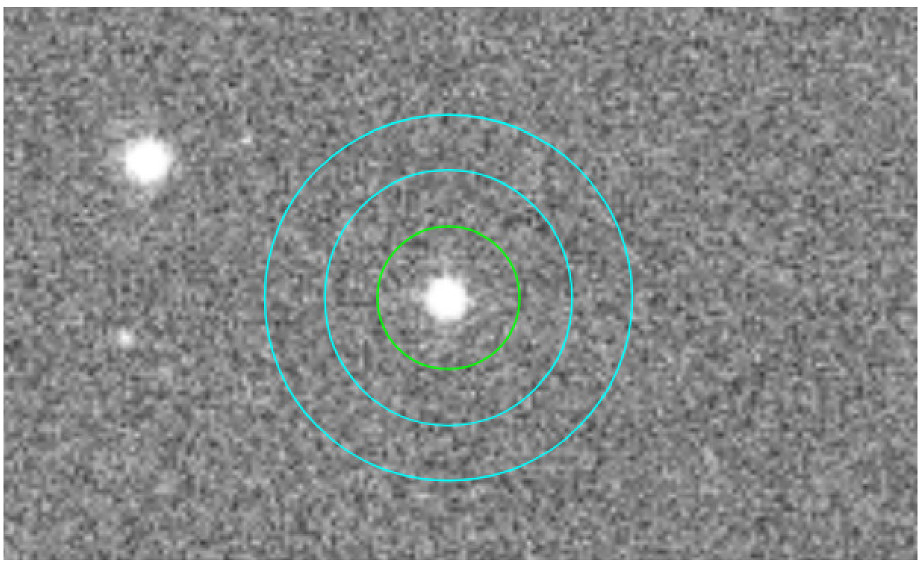

Figure 3.6: The aperture and annulus needed for performing background subtraction. The pixels inside the green area are used for measuring the flux of the star, and the pixels between the cyan rings are used for extracting the background flux.

Having an aperture size that is too large can be just as problematic as having a too small aperture. An oversized aperture measures the flux of more pixels, but also picks up more noise. Additionally, in a region with a high source density, another star can be inside the annulus or even inside the aperture of the target itself. On the contrary, undersized apertures often cannot compensate for variable PSF shapes. Consequently, when using a fixed-size aperture, it is customary to use an aperture size of about three times the FWHM of the point sources in an image. This size encloses a large fraction of the PSF while collecting a moderate amount of noise, and it was applied to all fixed-size aperture measurements taken in this thesis. Aperture photometry with fixed apertures has the advantage of being easy to perform, but is very sensitive to changes in the FWHM and other noise sources. In a more robust approach, aperture sizes are adapted for each image or even for each individual source. By measuring the FWHM of the stars in each image, an ideal aperture size can be calculated for every source during the observation. Since the FWHM of a star is slightly different in every image, the aperture size also varies. In Sect. 5.2.3, I present a comparison of fixed-size and adaptive-size apertures.

When photometry is performed from the ground, there are additional noise factors that complicate the detection process. The atmosphere is always in motion, and both turbulence and clouds can influence the result of photometric measurements. Seeing and scintillation are two of the main effects caused by atmospheric turbulence, whereas light absorption and scattering are the main problems from clouds. Additionally, the observed background emission is strongly influenced by the back-scattered light from street lamps. The variable background across the detector can be corrected by applying background subtraction or differential photometry.

The term differential photometry refers to the method of calculating the ratios of the flux of two or more stars. Dividing the flux of two stars mitigates many causes of transparency variations from frame to frame. Nevertheless, not all imaged stars are suitable for this process. In Fig. 3.7, stars highlighted in green refer to suitable candidates to perform photometry; for sources coloured orange, some precautions are required, while stars marked with a red circle cannot be used to reliably measure fluxes. In reference to this figure, the following list describes the method of differential photometry in more detail, where I will rank the sources according to their ability to be suitable reference stars (RS).

- **1:** This star is the main star, also called the target star, which might exhibit an exoplanet transit. It is located in the centre of the image, which in this case delivers the best signal-to-noise ratio.
- **2:** This star is located close to the target and has a similar brightness. Both of these properties potentially make it an ideal candidate for being a reference star.
- **3:** The brightness of the third star is slightly lower than that of the target star, and, additionally, it is at a greater distance from the target than star 2. As such, this source marks another useful reference candidate.
- **4:** This star is the brightest in the given image and therefore features, in principle, the best signal-to-noise ratio. However, for the integration time used, it is too bright, and pixels saturate near the centre of the PSF. This leads to a loss of photons in the

saturated area on the detector, and aperture photometry cannot be performed reliably. As a consequence, this star cannot be used as reference.

- **5:** Star number 5 is bright enough to be clearly distinguished from the background. As such, it might be possible to use it as a reference star. Nevertheless, this source is noticeably fainter than the target and would contribute a large amount of noise if used as a single reference. Furthermore, the star is located close to the edge of the detector, cutting off its PSF. As a consequence, this source cannot be used as reference object either.
- **6:** This star is very faint but very close to the target. Given these properties, this source can be a useful addition if combined with other reference stars.
- **7:** For this source, aperture photometry could be biased by the star in its immediate neighbourhood, therefore, biasing the flux measurements. With advanced extraction methods, such as fitting PSFs, a reliable flux measurement would be possible, in principle. However, this is beyond the scope of this thesis.

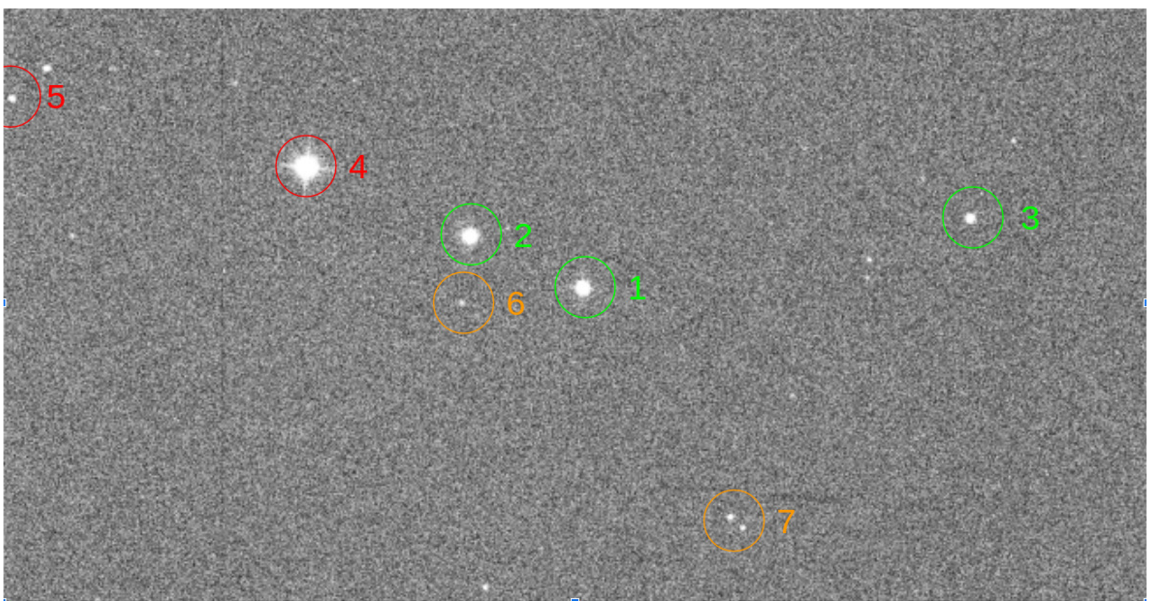

Figure 3.7: A cut-out of a processed light image from TOI1820 b (figure 4.3 h). The visible sources are highlighted in green, orange, and red, depending on their use-case for differential photometry.

Now that the selected star fluxes have been extracted from the processed frames, the 'differential' part of differential photometry can begin. This method creates an absolute difference without several error sources, such as clouds and variable atmospheric extinction, because they are very similar for both stars. In theory, if both stars are not variable and the relative difference is calculated for every image, the resulting light curve should be a straight horizontal line. However, if the brightness of one of the stars increases or decreases, the relative brightness changes as well. Differential photometry is therefore a widely used method for analysing variable star phenomena such as binaries (Wilson, 1994), evolved stars (Groenewegen, 2004) and exoplanets. In the case of exoplanet transit detection, differential photometry should be applied with the following logic: The flux of the exoplanet host star is divided by the measured flux of another star, the reference star. Applying this method to all images and plotting the results in a diagram displaying relative flux as a function of time diagram, any intrinsic brightness variations become visible. If the brightness of the target drops, the relative brightness of the light curves also decreases.

Using only one star as a reference can be problematic. If there are dominant noise sources coming from the flux of the reference star, this noise will propagate to the resulting light curve. By using multiple reference stars and creating a synthetic (averaged) reference star, less noise is propagated to the final light curve, and the possibility of outliers decreases. This is similar to the standard deviation formula (3.9). With more reference stars, the influence of each individual reference star, and hence, potential errors decrease.

$$std = \sqrt{\frac{\sum_{i=1}^{n} (x_i - \bar{x})^2}{n-1}} \tag{3.9}$$

With std being the standard deviation of the combined reference star, n the number of reference stars, x_i the flux of a single reference star, and $\bar{x}$ the arithmetic mean of the flux of the reference stars. The arithmetic flux mean can be calculated as follows:

$$\bar{x} = \frac{\sum_{i=1}^{n} x_i}{n} \tag{3.10}$$

An additional way to increase the quality of the final reference star is to weight the stars by their flux or standard deviation. Usually the stars with the highest flux have the best signal-to-noise ratio and therefore the best standard deviation, but random errors can always occur. It might be worth trying to weight via the standard deviation, but in this thesis the stars for the final reference star were weighted via the flux ratio. The formulas for the resulting weighted standard deviation and weighted arithmetic mean are as follows.

$$std^* = \sqrt{\frac{\sum_{i=1}^{n} w_i (x_i - \bar{x}^*)^2}{\frac{m-1}{m} \sum_{i=1}^{n} w_i}} \tag{3.11}$$

$$\bar{x}^* = \frac{\sum_{i=1}^{n} w_i x_i}{\sum_{i=1}^{n} w_i} \tag{3.12}$$

With std^* being the weighted standard deviation, w_i the weight of a single reference star, $\bar{x}^*$ the weighted arithmetic mean, and m the number of non-zero weights. The impact of some of these variables, for instance, the number of reference stars, will be presented and discussed in later sections. Finally, the visualised flux of an exoplanet transit is calculated as follows.

$$F_n = (F_t/\bar{F}^*)/a \tag{3.13}$$

With F_n being the normalised differential flux of the target star, F_t the flux of the target star, $\bar{F}^*$ the weighted synthetic reference star, and a a factor to normalise the light curve to unity outside the dip.

3.3 Planning of Observations

One of the most important tasks of an observing astronomer is planning the observation night. Here, the most essential item is to ensure that no unnecessary or unexpected distractions may disturb a successful prosecution of an observation night. Since telescope time can be very expensive, it is crucial to make sure that every minute is well spent and that the observation goes according to schedule. Another important aspect is safety, as a weather change can cause severe damage to a telescope. There are many meteorological and astronomical factors to be watched out for, but there are fortunately many methods to plan and ensure that the observation session is successful. Regardless of the scenario, all require careful preparations to successfully record the necessary data. For this thesis, the planning of the observations for this specific project is discussed.

There are several websites that highlight interesting targets and can help to find the optimal date to observe them. One of the websites used for this thesis is the Exoplanet Transit Database (ETD)[2], which covers most known exoplanets with detailed predictions. As of September 27th 2022, there are 450 exoplanets listed on the website, and most of them have been detected multiple times. Another important website was the transit alert page of TESS[3], since TESS is the latest exoplanet hunting space telescope and is still operating at the moment. Currently, there are nearly 6000 transit alerts displayed on the webpage with many details about the exoplanet candidate and its host star. However, not all of these alerts are exoplanets. There are many false positives, and knowledge about the survey instrumentation and host star enables one to better isolate the most promising targets for follow-up observations. NASA uses its own time system specifically for TESS, and to be able to know when the next transit of an exoplanet occurs, the time tables have to be transformed into local time. To make things easier, the Kuffner Observatory Club

[2] http://var2.astro.cz/ETD/
[3] https://tess.mit.edu/toi-releases/

created a website[4] for TESS transits that are possible to be observed from Austria with all the necessary information. An example of such a transit prediction table from the Kuffner Observatory Club is presented in Fig. 3.8.

TOI	Typ [TESS]	mag_T	Ing. [UTC]	Mid-Transit [UTC]	+/- [h]	Egr. [UTC]	h [°]	Az [°]	D [h]	d [%]	Peri [d]	h_So [°]	Vis [h]	Con [IAU]	RA J2000 [°]	Dec [°]
5198.01	PC	12.0	22:10	05-15 23:38	0.0	01:05	74	87	2.9	0.85	3.3	-22	8.8	Her	266.56	46.50
1303.01	PC	9.9	22:20	05-15 23:42	1.9	01:05	52	72	2.8	0.17	1.6	-22	8.8	Cyg	301.72	45.50
5244.01	PC	12.8	21:37	05-15 23:45	0.0	01:52	53	59	4.2	0.49	5.1	-22	8.8	Cyg	305.26	52.91
5189.01	PC	12.9	22:21	05-15 23:58	0.0	01:35	45	358	3.2	0.91	9.5	-21	8.8	Cep	94.08	87.32
2106.01	PC	9.9	23:33	05-15 23:59	0.4	00:25	61	279	0.9	0.12	0.6	-21	8.8	CVn	207.18	44.91
1834.01	PC	11.5	00:01	05-16 01:03	0.5	02:04	40	274	2.0	1.48	1.2	-17	8.8	CVn	202.29	31.40
1442.01	PC	12.5	00:47	05-16 01:03	0.2	01:19	62	12	0.5	0.16	0.4	-17	8.8	Dra	287.29	74.17

Figure 3.8: Examples of TESS alerts from the Kuffner Observatory Club TESST programme. In this database, the time, position, and depth of the transit is displayed. Additionally, the website includes comments on each alert, hinting at false-positive detections from TESS.

After having an arsenal of potential targets, the next step was a test run to see if detecting an exoplanet is possible under the present conditions. For that a well-known and easy-to-observe exoplanet had to be chosen to get a first evaluation of the capability of the telescope and to be able to start programming the software for data reduction, photometry, plotting, and statistics. Fig. 3.9 shows that an exoplanet transit with the Nordkuppel telescope has already been detected in the past.

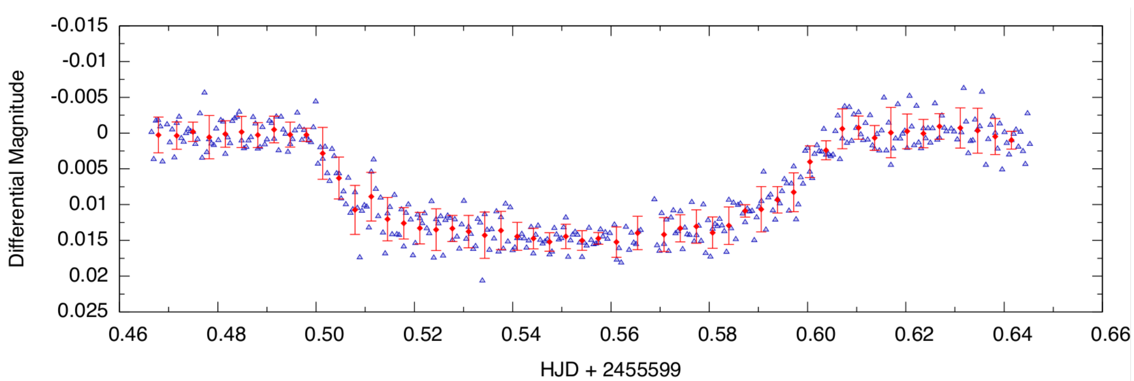

Figure 3.9: An exoplanet transit of XO-2B b observed by Stefan Meingast with the Nordkuppel telescope observed on February 6th 2011. On the y-axis is the differential magnitude of the target against the reference stars and on the x-axis is the date displayed. The blue rectangles are the individual data points. The red squares are the running mean with bars indicating the local standard deviation.

[4] http://info.plato-planeten.at/

To find an accessible target for the geographic location of the telescopes, I queried the ETD for exoplanet transits that met the following criteria.

- **Brightness:** In order to find a target suitable for both telescope systems, I required the target to be brighter than 13 mag. Within this limit, observations with both telescopes would require less than about 1 minute of integration time, and, moreover, most TESS targets are restricted to this limit for optimal data quality (Huang et al., 2020).

- **Transit Depth:** To ensure the detectability of the transit, I required a minimum transit depth of at least 0.5 %. In practise, this threshold needs to be set in relation to the target brightness and the availability of the reference stars to achieve the required signal-to-noise ratio in the light curves.

- **Altitude:** The longer the path through the atmosphere of a light beam, the more turbulence it encounters. To mitigate this effect, the observed targets should be as close to the zenith as possible, due to the smaller airmass. Therefore, the minimum altitude of the target was set at 40°. In the formula for the scintillation approximation (Young, 1967) - the noise coming from the atmospheric turbulence - the dependence on the airmass / altitude is visible.

$$\sigma = 0.09\ D^{-2/3}\ sec(Z)^{1.75}\ e^{-h/h_0}\ t^{-0.5} \tag{3.14}$$

  where σ is the scintillation RMS in units of relative intensity (Dravins et al., 1998), D is the aperture diameter, Z is the altitude, h is the height above mean sea level of the telescope, h_0 is 8000 m and t is the integration time. Another factor for altitude restriction is the mechanical limit of the telescopes. Both telescopes should not be operated below 30° altitude and, to ensure safety during observations, an additional 10° was added.

- **Reference Stars:** To be able to perform differential photometry, there must be at least one reference star. For quality reasons, the minimum number of reference stars for the Nordkuppel field of view was set to five, although with its massive field of view there are usually way more reference stars inside. Additionally, it is important that the reference star has a brightness similar to that of the target star. If it is too faint, it produces too much noise. If it is too bright, it limits the integration time of the target. Hence, I decided that the reference stars should be within approximately two magnitudes of the target star. To be able to observe the transit with the Figl, at least one reference star needs to be at a distance of 3' from the target. Since the field of view of the Figl telescope is smaller by a factor of 35, it is not easy to find an exoplanet host star with another star of similar brightness at a distance of 3'. The difference in potential reference stars between the Nordkuppel and Figl telescopes is shown in Fig. 3.10 :

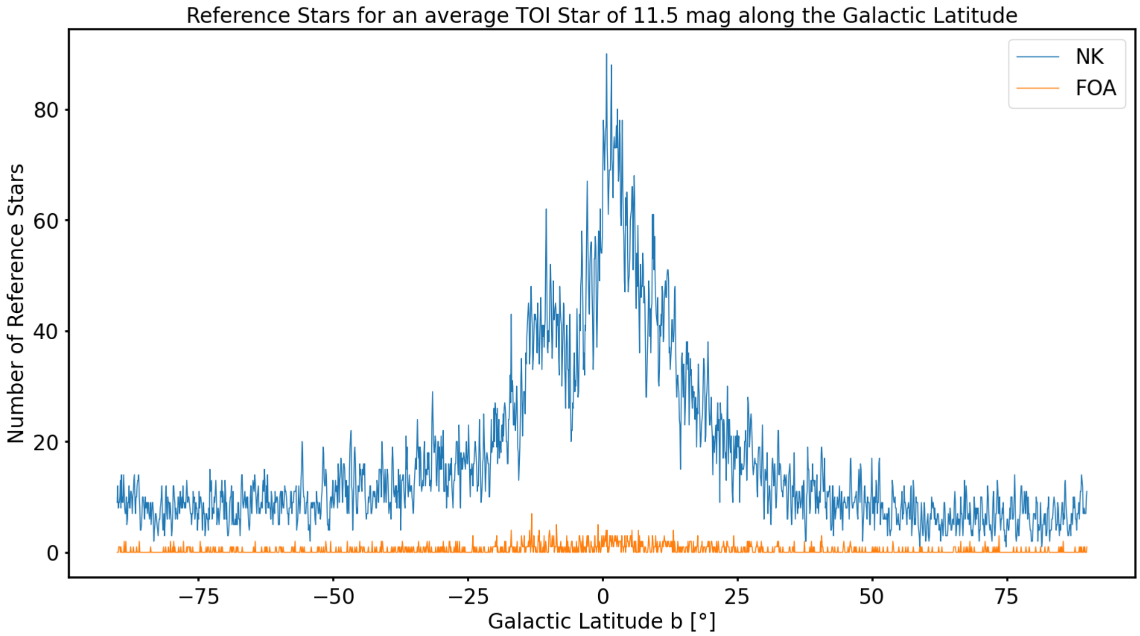

Figure 3.10: The amount of available reference stars for the Figl and Nordkuppel setups when scanning the sky along the galactic latitude b at l = 0°. On the y-axis the number of reference stars is displayed. On the x-axis the galactic latitude, from the galactic north-pole (left) to the galactic south-pole (right), is displayed.

The diagram in Fig. 3.10 was created by scanning the Gaia DR2 catalogue (Gaia Collaboration et al., 2018) along the galactic latitude with a fixed longitude of l = 0°. For the Nordkuppel telescope, an 18’ x 18’ window was used, and for the Figl telescope, a 3’ x 3’ window was used. All stars with a brightness of 11.5±2 mag in the R band were accumulated and plotted against its position. 11.5 mag is the median brightness of a TESS exoplanet host star (Ricker et al., 2015). On average, there are 17.1 stars in a Nordkuppel field of view and 0.46 stars for the Figl telescope. The ratio for those values is 37.3, which is nearly the same as their field of view ratio. Since on average there is not even a single star with a brightness of 9.5-13.5 mag in the field of view of the Figl, it is not possible to rely on the existence of suitable reference stars.

- **Spectral Class:** Stars that are too blue are less interesting for exoplanet detection because they are too active and, therefore, sometimes variable (Marcy et al., 2005). Therefore, the spectral class range for the target star should be in the range of an F5 - M star. The reference stars should have similar spectral types, as shown in Sect. 5.2.1.

- **Sun Altitude:** When the sun sets, the sky is not completely dark, since some of the light rays still illuminate the sky due to different optical and atmospheric phenomena, for example wavelength-dependent refraction (Patat et al., 2006). There are three twilight phases after sunset: If the Sun is below $-6°$ it is called civil twilight, below $-12°$ it is called nautical twilight, and when the Sun is below $-18°$ the sky is in the so-called astronomical twilight phase without more influence of the Sun. High-precision photometry should only be performed after nautical twilight. However, differential photometry can be performed at earlier phases, but it depends on the brightness of the target.

- **Moon Phase**: The moon is the brightest object at night. Ideally, the observation takes place during the time of a new moon. If visible, the increased background flux from scattered moon light introduces more noise in the recorded flux and will therefore decrease the quality of the observations. A full moon next to the target would prevent any observations.

- **Variability:** Since the core phenomena for the transit method involve extrinsic brightness variability, it is disadvantageous if the target star or a reference star is intrinsically variable. To avoid propagating variable signals when performing differential photometry, all stars should be checked in advance and should be investigated individually when computing the differential flux.

The following websites were used to check for transits listed in the ETD: SIMBAD[5] to check luminosities, reference stars, spectral class and variability, as well as Stellarium software [6] to check altitude, reference stars, sun height, moon phase, and the position of the target. After scanning all those websites, multiple potential candidates were found on ETD, and the next step was to find a night when the ephemeris and weather were adequate for a test run. The first observations took place in the night from February 25th to 26th 2021, with the target being WASP-11b. Although there was almost full moon at this time, the target was several tens of degrees away from the moon. After this session, I started writing the software and planning the next observation. The dual observation was planned slightly differently, but overall the same schematics were used. This time, the plan was to reserve a week, 10-16 May, due to the new moon and to get as many observations done as possible. On the first night, the weather was almost perfect and TOI 1820 b and HAT-P-36 b were observed. Since TOI1820 b was an unconfirmed TESS object at the time of the observations, this object was assigned a higher priority to obtain the full transit. Given the difficult weather situation, thorough planning of the observations ensured that at least these two nights in February and May were successful.

[5] http://simbad.u-strasbg.fr/simbad/
[6] https://stellarium.org/en/

3.4 Software

To analyse the collected data, several software applications and programming languages were used. Some I developed myself in Python, but many applications were adopted from other sources. The following list briefly describes the software used.

- **Python**: The programming language used for this thesis to perform data science. The main packages used are astropy (Astropy Collaboration et al., 2013), numpy (van der Walt et al., 2011), scipy (Virtanen et al., 2020), matplotlib (Hunter, 2007), photutils (Bradley et al., 2020), sklearn (Pedregosa et al., 2012), epehm (Rhodes, 2011), and astroquery (Ginsburg et al., 2019).
- **Source Extractor**: This command-line utility developed by Bertin & Arnouts (1996) for source extraction and characterisation was used for aperture photometry. Specifically, the parameters that I recorded were: X_IMAGE and Y_IMAGE for the position of the stars, FLUX_APER for fixed-sized apertures, FLUX_AUTO for adaptive-sized apertures, BACKGROUND for background values and FWHM_WORLD for full width have maxima.
- **Siril and DS9**: Siril[7] and SAOImageDS9 (Smithsonian Astrophysical Observatory, 2000) were mainly used to display frames and analyse the PSF and FWHM of the point sources.
- **TOPCAT**: This programme for data and table management developed by Taylor (2005) was used to perform table operations, and specifically cross-matching.
- **Stellarium**: I used this programme to visualise the neighbourhood of the targets and their ephemeris.

[7] https://siril.org/

Chapter 4

Observations and Data

This chapter provides an overview of the different observations and the data collected. Two observation sessions were organised and executed, first a test session and then a dual observation to obtain a robust evaluation of the two telescopes. The first observation was made with the Nordkuppel telescope and was intended as a test run to ensure the possibility of detecting exoplanets. Furthermore, this first run was important because scripts for data reduction, photometry, and plotting could be developed in advance of the dual observation. For the second observing night, the Nordkuppel telescope and the Figl telescope were used simultaneously, targeting the same objects to get a reliable comparison between the two setups. In the following sections, I present the observed targets and observational parameters, as well as the collected data and data processing.

4.1 Objects

WASP-11 b was the first exoplanet observed for this thesis and was intended to be the test run for the evaluation project. The transit from WASP-11 was already well-determined (West et al., 2009; Sada et al., 2012) and the exact timing was extracted from the ETD. The target turned out to be an ideal test object for the start, since it has a deep transit depth of 2.5 %.

During the second observation session, it was possible to catch two transits back-to-back with both the Nordkuppel and the Figl simultaneously. First, the full transit of TOI1820 b, also known as Melotte 111 AV 1961, was observed and the egress of HAT-P-36 b was also successfully detected. TOI1802 b was a transit alert target of the TESS follow-up programme; therefore, it was not clear whether detection of the target transit was even possible. This is because the errors of unconfirmed exoplanets, especially the timing, can be quite large. However, the expected transit parameters were ideal for mea-

suring the photometric limits of the available instrumentation. Fortunately, with HAT-P-36 b, another confirmed exoplanet (Bakos et al., 2012), a reliable target for the comparison of the two telescopes was identified. Finding those two successive transits on the same night was fortunate because the small field of view of the Figl telescope usually makes it challenging to find a good reference star for differential photometry.
The astrophysical parameters of the stars and their planets were determined by many previous publications[1] [2] [3] and are displayed in Tab. 4.1.

Table 4.1: The astrophysical parameters of the stars WASP-11, TOI1820, and HAT-P-36 and their observed planets. Note that the exoplanet parameters are estimates and can exhibit large (systematic) errors. The masses of the stars were calculated with the mass-luminosity relation (Equ. 4.1; Kuiper, 1938).

Star Parameter	WASP-11	TOI 1820	HAT-P-36
Alternative Names	HAT-P-10	Melotte 111 AV 1961	TYC 3020-2221-1
Spectral Type	K3	G5	G6
Gaia Magnitude	11.56 mag	10.96 mag	12.08 mag
ICRS Right Ascension	03h 09m 28.54s	12h 30m 44.75s	12h 33m 03.90s
ICRS Declination	+30° 40’ 24.86”	+27° 27’ 07.72”	+44° 54’ 55.19”
Distance	130 pc / 7.6997 mas	260 pc / 3.8403 mas	294 pc / 3.4055 mas
Color Index B-V / B-R	+1.01 / +1.22	+0.35 / +0.84	+0.37 / +0.89
Temperature	4834 K	5620 K	5476 K
Radius	0.81 $R_\odot$	1.47 $R_\odot$	1.10 $R_\odot$
Luminosity	0.32 $L_\odot$	1.938 $L_\odot$	0.979 $L_\odot$
Mass	0.75 $M_\odot$	1.18 $M_\odot$	0.99 $M_\odot$
Absolute Magnitude	5.99 mag	3.88 mag	4.74 mag
Exoplanet Parameter	WASP-11 b	TOI 1820 b	HAT-P-36 b
Transit Depth	2.54 %	0.58 %	1.59 %
Transit Duration	159 min	163 min	133 min
Transit Period	3.722469 days	4.86071 days	4.17524 days

$$\frac{L}{L_\odot} = \left(\frac{M}{M_\odot}\right)^a \tag{4.1}$$

With L being the luminosity of the star, $L_\odot$ the luminosity of the sun, M the mass of the star, $M_\odot$ the mass of the Sun, and a an exponential factor, depending on M (Salaris & Cassisi, 2005). The distance modulus is given by

$$m - M = 5\ log_{10}(d) - 5, \tag{4.2}$$

[1] https://simbad.u-strasbg.fr/simbad/sim-id?Ident=WASP-11
[2] http://simbad.u-strasbg.fr/simbad/sim-id?Ident=HAT-P-36
[3] http://simbad.u-strasbg.fr/simbad/sim-id?Ident=Cl*+Melotte+111+AV+1961

with m being the apparent brightness, M the absolute brightness, and d the distance. With this relation, the absolute magnitudes of the target stars were calculated and placed in the Gaia HRD in Fig. 4.1.

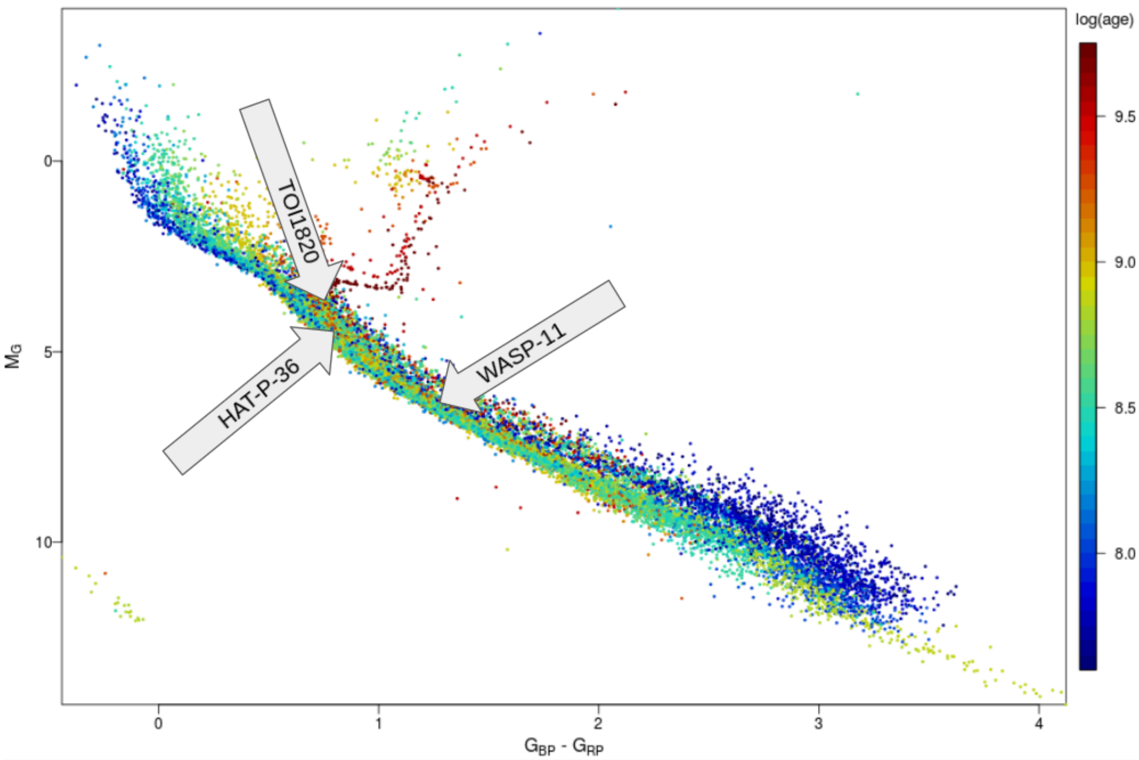

Figure 4.1: The Hertzsprung-Russel diagram from Gaia DR2 (Gaia Collaboration et al., 2018) with the three target stars marked with arrows. All target stars are located on the main sequence.

4.2 Observations

The first set of observations took place at the Nordkuppel on February 25th 2021 with the goal of catching the transit ingress of WASP-11 b. To guarantee capturing this event, I started taking data in the V band already one hour before the expected start of the transit. The observation started at 17:34 UTC (18:34 MEZ) and ended at 19:41 UTC (20:41 MEZ) without interruption. Although there was almost full moon with the fraction of lunar illumination (FLI) at 97%, the distance of the moon to the target star was far enough (about 85°) so that the increased background brightness did not influence the observation critically. The large moon brightness will be discussed further in Chapter 5. In addition to the bright moon phase, some clouds were also present during the observations.

The second observing run took place on the night of May 10th 2021 and was performed with the Figl and Nordkuppel telescopes simultaneously. Both observations were made from the Institute of Astrophysics, since the Figl observatory can be controlled remotely. However, it was not possible to observe the full transits for both objects because they overlapped. Following the transit of TOI1820 b, the egress phase of the transit of HAT-P-36 b was scheduled. During this night, the moon phase was not a worrying factor, and also the weather conditions were stable with mostly clear skies. Additionally, this time the observations were made in the R passband. An overview of all the setup of the observations can be found in Tabs. 4.2 and 4.3.

Table 4.2: The observation setup for the target observed with the Nordkuppel telescope.

Observations NK	WASP-11 b	TOI 1820 b	HAT-P-36 b
Date	February 25th 2021	May 10th-11th 2021	May 10th-11th 2021
Time	17:34 - 19:41 UTC	19:06 - 23:30 UTC	23:43 - 01:00 UTC
Exposure Time	30 s	15 s	25 s
Filter	Bessel V	Bessel R	Bessel R
Binning	2x2	2x2	2x2
Sensor Temperature	-15° C	-15° C	-15° C
Average FWHM	2.99"	2.21"	2.87"
FWHM Range	2.42" - 4.00"	1.60" - 3.58"	2.18" - 3.53"
FLI	97 %	1 %	1 %
Moon Distance	85°	135°	150°
Airmass	1.13 - 1.49	1.09 - 1.39	1.24 - 1.49
Sun Altitude	-11° - -31°	-7° - -23°	-22° - -18°
Number of Light Images	235	888	169

Table 4.3: The observation setup for the objects observed with the Figl telescope.

Observations FOA	TOI 1820 b	HAT-P-36 b
Date	May 10th-11th 2021	May 10th-11th 2021
Time	19:29 - 23:33 UTC	23:43 - 00:49
Exposure Time	30 s	30 s
Filter	Bessel R	Bessel R
Binning	none	none
Sensor Temperature	0° C	0° C
Average FWHM	2.50"	2.95"
FWHM Range	1.78" - 3.71"	2.21" - 3.61"
FLI	1%	1%
Moon Distance	135°	150°
Airmass	1.08 - 1.39	1.24 - 1.39
Sun Altitude	-10° - -23°	-23° - -19°
Number of Light Images	447	124

4.3 Data

This section provides an overview of the data collected during the observing nights, starting with those to remove the instrumental signature, including bias, dark, and flat frames, and images of the science targets. In the following paragraphs, all steps in the data reduction process are listed consecutively.

Table 4.4: Number of images taken for all observations. The images required for data processing were recorded before the observation session in all cases.

Observation	Bias	Darks	Flats	Lights
NK WASP-11 b	20	20	9x5s, 15x7s, 5x15s	235
NK TOI1820 b	50	50	5x4s, 5x10s	888
NK HAT-P-36 b	50	50	5x4s, 5x10s	169
FOA TOI1820 b	10	10	10	447
FOA HAT-P-36 b	10	10	10	124

- **Bias**: A bias frame is taken by recording an image with zero seconds integration time. These data primarily represent the read-out noise, but also highlight dead pixels. As the name suggests, the noise components of this type of image can be found in all other data taken with the same detector.

- **Dark**: The dark current is a small temperature-dependent electrical current resulting from spontaneously generated charge. This effect linearly increases with time and therefore is cancellable if recorded and applied correctly to the science frames. When taking a dark frame, there is, similar to the bias frame, no external illumination since the shutter to the sensor remains closed. For this process, the integration time ideally is identical to the light frames, but the dark current can be scaled when bias frames are also taken.

- **Flat**: To create a flat field, an image of a homogeneously illuminated surface is taken for each passband separately. This can be achieved by taking images of the twilight sky or with lamps that illuminate a suitable surface inside the dome structure. The recorded flat field is sensitive to any asymmetries in the illumination of the detector arising from, e.g. vignetting or dust particles on the surface of optical elements.

- **Light**: The light or science field is the image of the object of interest. To remove the instrumental signature from these frames, the above-mentioned files are required for proper removal of the instrumental signature.

The application of the collected frames required to process the science images is as follows. First, the bias frames are combined with a median to create a master bias frame. The reason why I preferred the median as combination metric as opposed to an average is that the median effectively removes outliers. Next, the master bias is subtracted from the recorded dark frames, leaving mainly the dark current. These preprocessed dark frames are combined with median to create a master dark image that measures the detector's dark current. This approach allows one to apply a scaling factor to the dark current in case the dark images do not feature the same integration time as the light frames. For the master flat, the master bias and the (scaled) master dark are initially subtracted from the individual flat fields. The resulting frames are then scaled to unity and then again combined with a median. After creating the master images with the recipes described above, they can be applied to the science data following the relation

$$(Raw - M_{Bias} - DC \cdot t)/M_{Flat} = Corr \tag{4.3}$$

with Raw being the uncorrected light image, M_{Bias} the Master Bias, DC the dark current, t the exposure time, M_{Flat} the Master Flat, and $Corr$ the corrected light image.

Figs. 4.2, 4.3, 4.4 and 4.5 show the data processing steps for the objects WASP-11 b, TOI1820b, and HAT-P-36 b, respectively. Most of the systematic errors were corrected, but by stretching the data values some flaws were still visible. For example, in 4.2 (h) some dust doughnuts can be detected. Also in the corrected Figl data there is still a vertical bar from the bias. See 4.4 (d) for the bias and (h) for the corrected light image with a faint vertical bar in the centre. It should be noted that the calibration images for data collected with the Figl telescope were transposed with respect to the light frames, as visible in Figs. 4.4 (c) and (g).

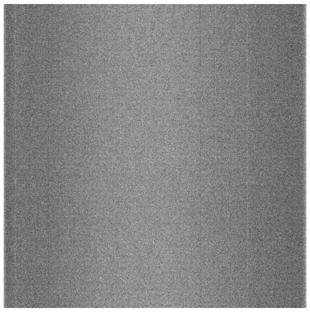

(a) Raw Bias

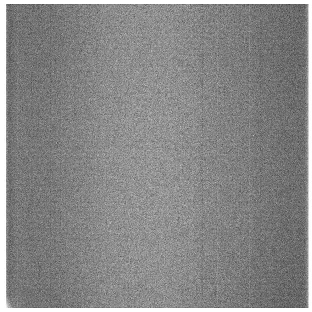

(b) Raw Dark

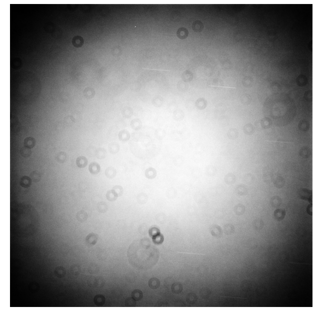

(c) Raw Flat

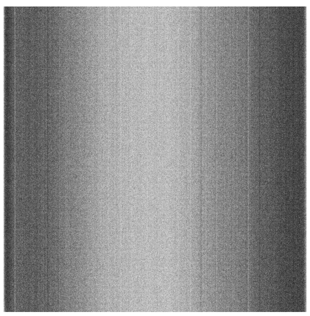

(d) Master Bias

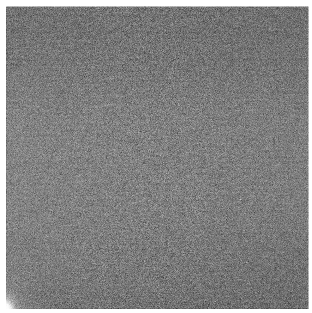

(e) Master Dark

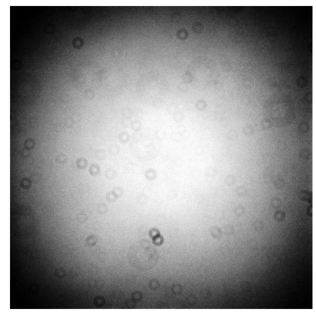

(f) Master Flat

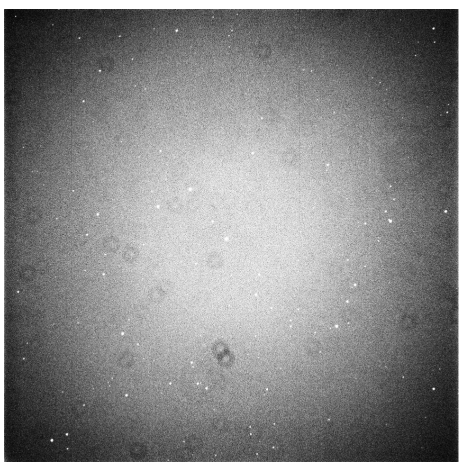

(g) Raw Light Dark

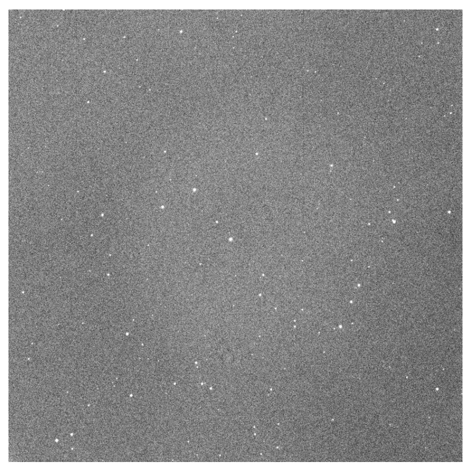

(h) Corrected Light

Figure 4.2: Images for the WASP-11 b observation with Nordkuppel. In the first row, the unedited bias, dark, and flat images are presented (a,b,c), and directly below are their master counterparts (d,e,f). In the bottom row, there is a light image before (g) and after (h) data processing.

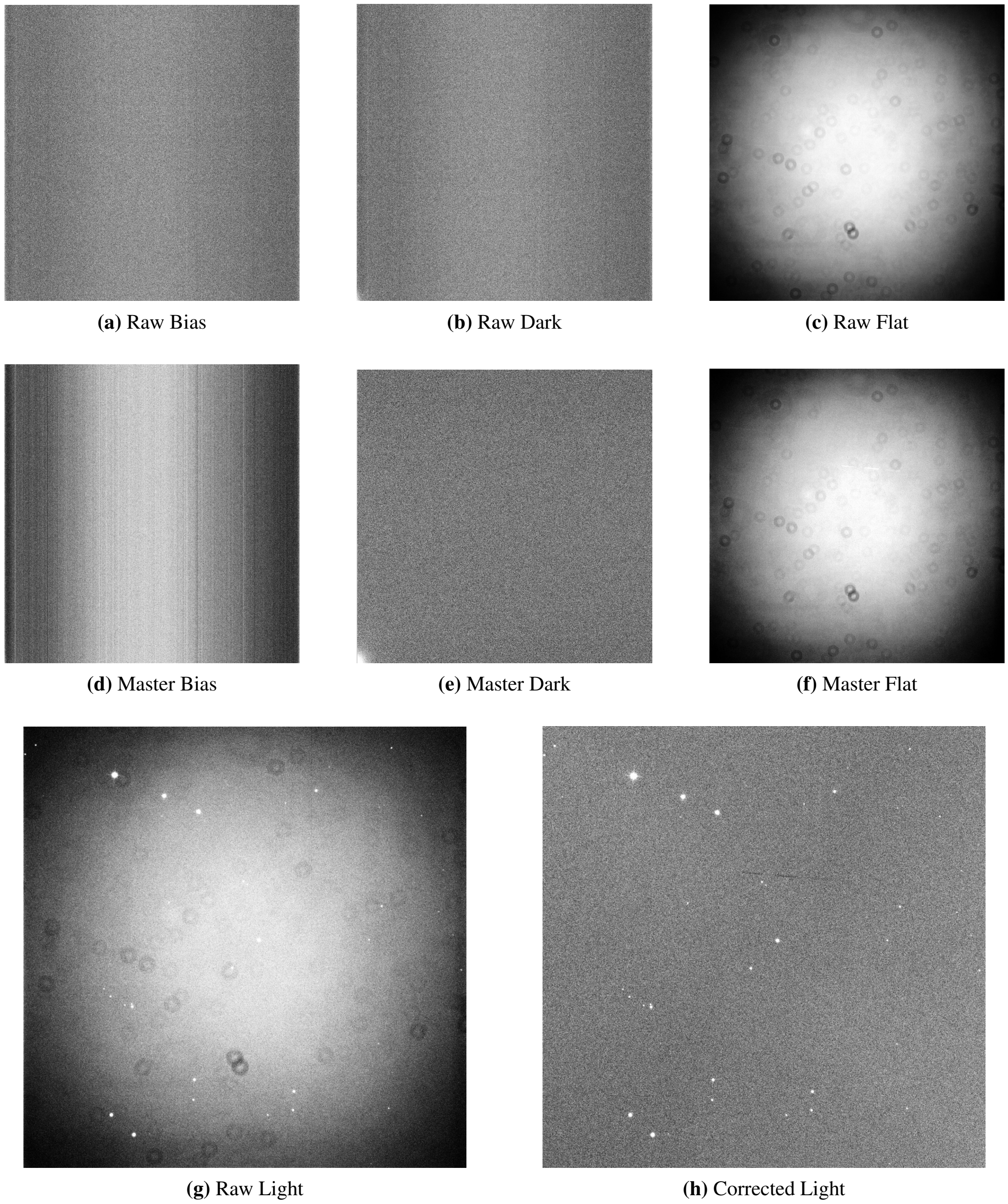

Figure 4.3: Images for the TOI1820 b observation with Nordkuppel. In the first row, the unedited bias, dark, and flat images are presented (a,b,c), and directly below are their master counterparts (d,e,f). In the bottom row, there is a light image before (g) and after (h) data processing.

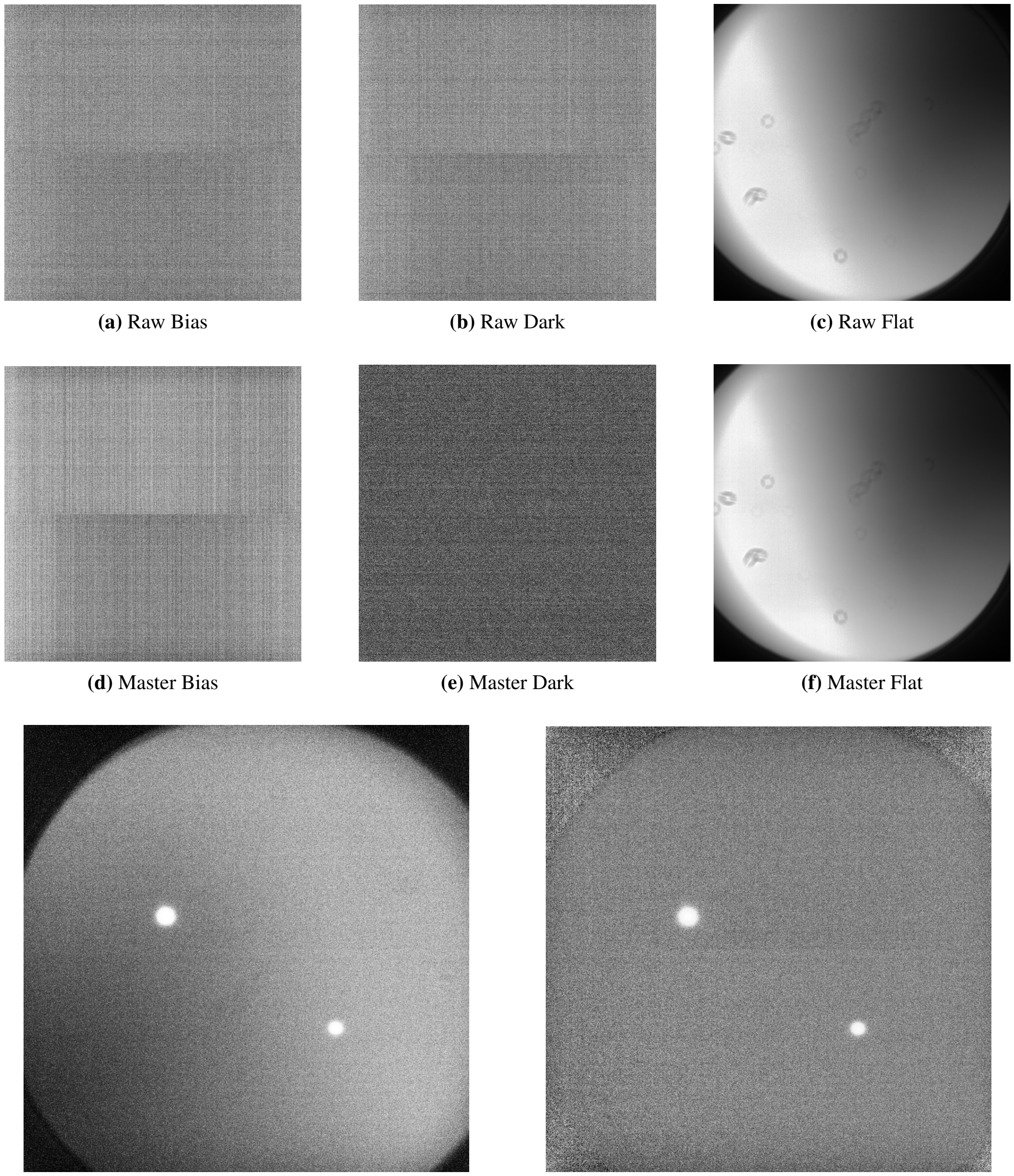

(a) Raw Bias (b) Raw Dark (c) Raw Flat

(d) Master Bias (e) Master Dark (f) Master Flat

(g) Raw Light (h) Corrected Light

Figure 4.4: Images for TOI1820 b observation with Figl. In the first row, the unedited bias, dark, and flat images are presented (a,b,c), and directly below are their master counterparts (d,e,f). In the bottom row, there is a light image before (g) and after (h) data processing.

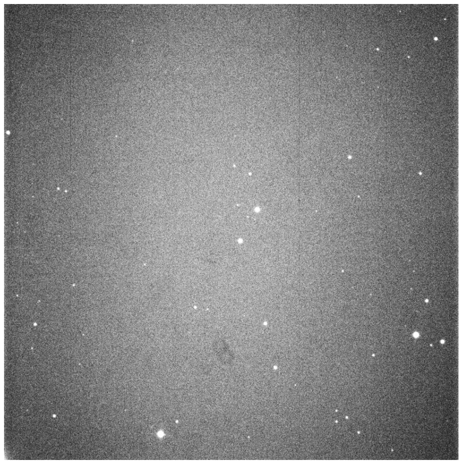

(a) Raw Light

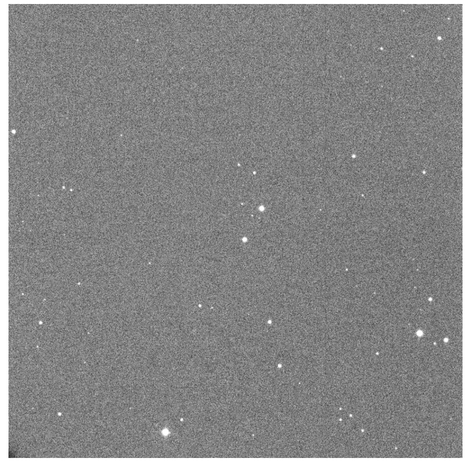

(b) Corrected Light

(c) Raw Light

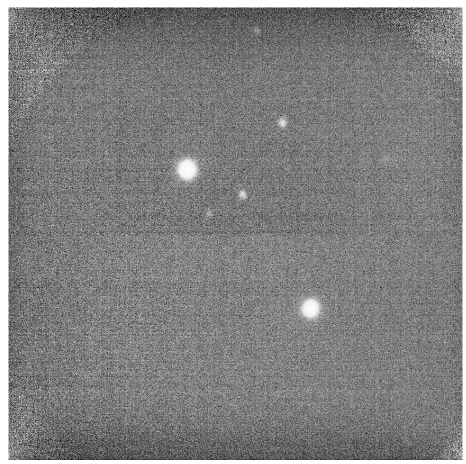

(d) Corrected Light

Figure 4.5: Images for the HAT-P-36 b observation with Nordkuppel and Figl. In the first row, there is a light image of the Nordkuppel (a) before and (b) after data reduction. In the second row, there is a light image of Figl (c) before and (d) after data processing. Since the observation for HAT-P-36 b took place right after TOI1820 b, the same bias, dark, and flat images were used. For this observation, only the raw and corrected light images are displayed.

Chapter 5

Results

In this chapter, I present the results of this thesis. First, the observations are visualised with light curves and diagrams. In the next section, a statistical evaluation was performed, including a noise analysis. Also, the astrophysical parameters of the exoplanets are calculated from the obtained data and compared with those in the literature.

5.1 Observations

The plotting style used in the following sections is identical in all diagrams. Each blue dot is the differential flux of the target; the light blue dots are outside the 2.5-sigma range and were clipped. The yellow area is the running standard deviation. The literature depth of the exoplanet transit is plotted in grey.

5.1.1 WASP-11 b

The first observation targeting WASP-11 b was made with the Nordkuppel telescope and analysed using Python only with fixed-sized apertures. For this transit, only the ingress was captured and the light curve of Fig. 5.1 was created with ten reference stars. The published depth of the transit of WASP-11 b is 2.54 % (see Tab.4.1) but, as visible in this figure, the measured depth is nearly 4 %. The median standard deviation is 0.44 % with a range of 0.31 % to 0.77 %. The humps at Julian dates of 2459271.26 JD and 2459271.29 JD could be explained by highly variable weather conditions. Note that the photometry software was further developed and adapted throughout the thesis. Therefore, the quality of the data analysis for WASP-11 b may not be as good as for TOI1820 b and HAT-P-36 b.

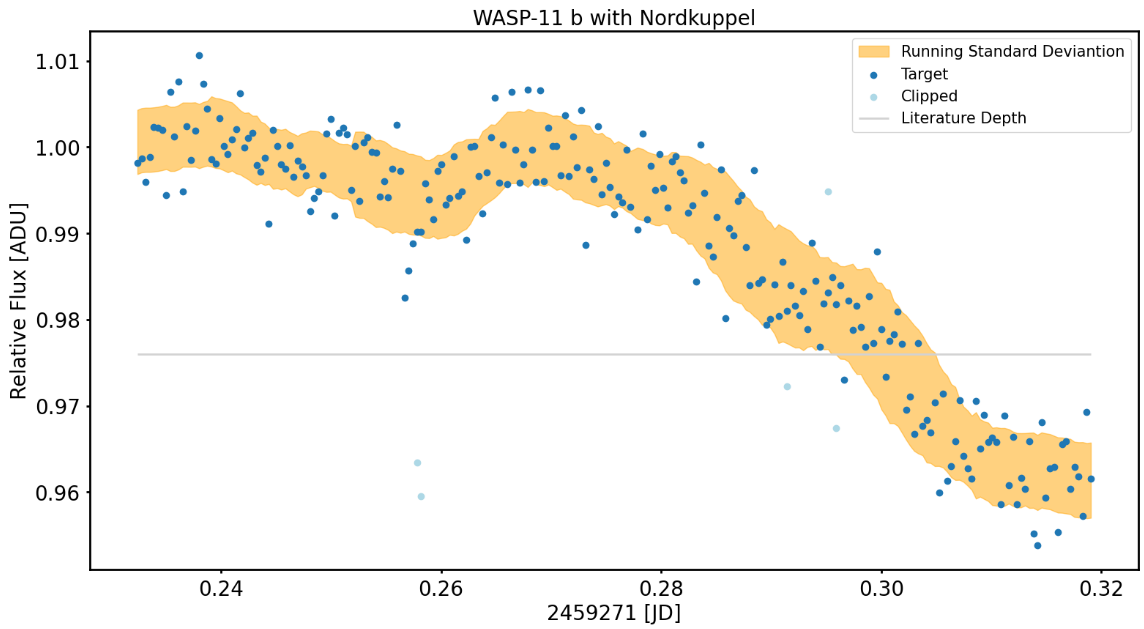

Figure 5.1: The light curve of the ingress of WASP-11 b as observed with Nordkuppel. On the x-axis, the Julian Date is displayed, and on the y-axis the normalised relative flux is displayed. The observation took place on February 25th 2021, and lasted for 130 minutes. The exposure time is 30 s with a target brightness of 11.5 mag. The transit is clearly visible, starting at JD 2459271.27 with an approximate depth of 4%.

5.1.2 TOI1820 b

TOI1820 b was the first target of the dual observation. Source extraction and photometry was performed with Source Extractor from here on. Fig. 5.2 shows the TOI1820 b transit light curve with the Nordkuppel telescope. Using ten reference stars, the published depth of 0.64 % (Knudstrup et al., 2022) was matched quite well. The median standard deviation is 0.35 % with a range of 0.22 % to 0.49 %. In the right-hand part after the egress, the target seems to get fainter. This was not expected, since the brightness of the stars should be stable after the transit. However, for an in-depth discussion of this effect, the observation would have to cover a longer time span. The noise is not significantly different throughout the transit, see Fig. 5.13.

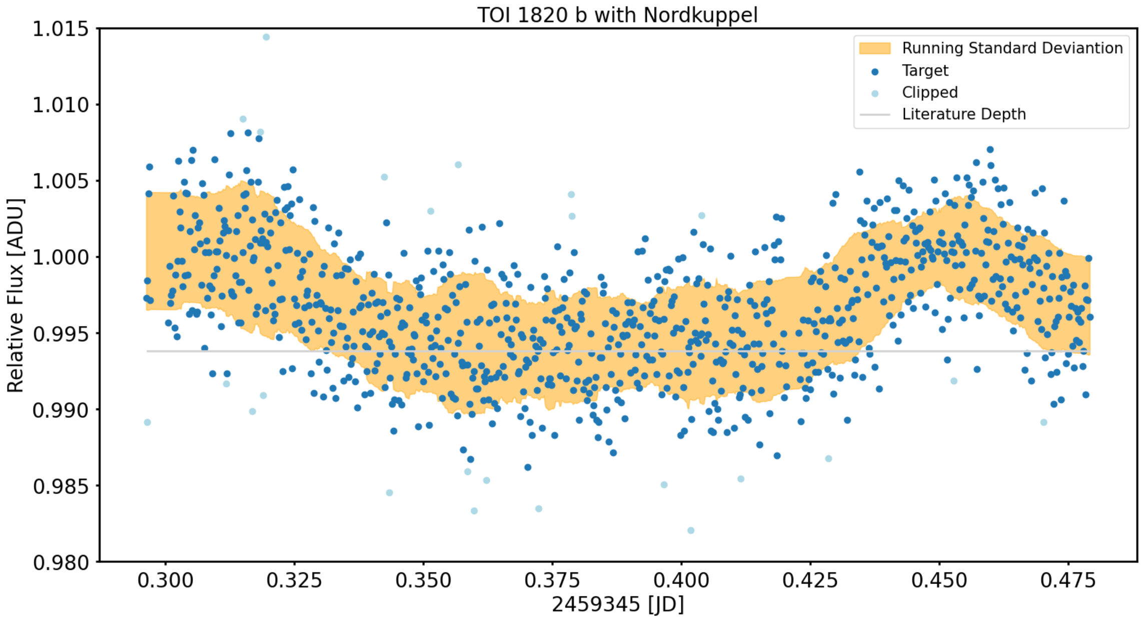

Figure 5.2: The light curve of the full transit of TOI1820 b with Nordkuppel. On the x-axis, the Julian Date is displayed, and on the y-axis the normalised differential flux is displayed. The observation took place on May 10th 2021 and lasted for 270 minutes. The exposure time is 15 s with a target luminosity of 11 mag. The complete transit is clearly visible, starting at JD 2459345.315 and ending at JD 2459345.455 with a depth of approximately 0.6%.

The transit of TOI1820 b observed with the Figl telescope looks different compared to the light curve observed with the Nordkuppel telescope, as can be seen in Fig. 5.3. Since there was only one reference star, which was significantly fainter than the target, the noise level with Figl was higher compared to the noise of the Nordkuppel, with a median standard deviation of 0.51 % within a range of 0.29 % to 0.62 %. The hump in the middle of the transit is notable at about JD 2459345.400. The weather conditions had a temporal change during that time, visible in the FWHM Fig. 5.14, which might have an influence on the photometric quality. The photometry with fixed-size apertures applied to this light curve was pure noise with a huge brightness gradient, and will not be shown. However, with Source Extractor the transit was at least visible.

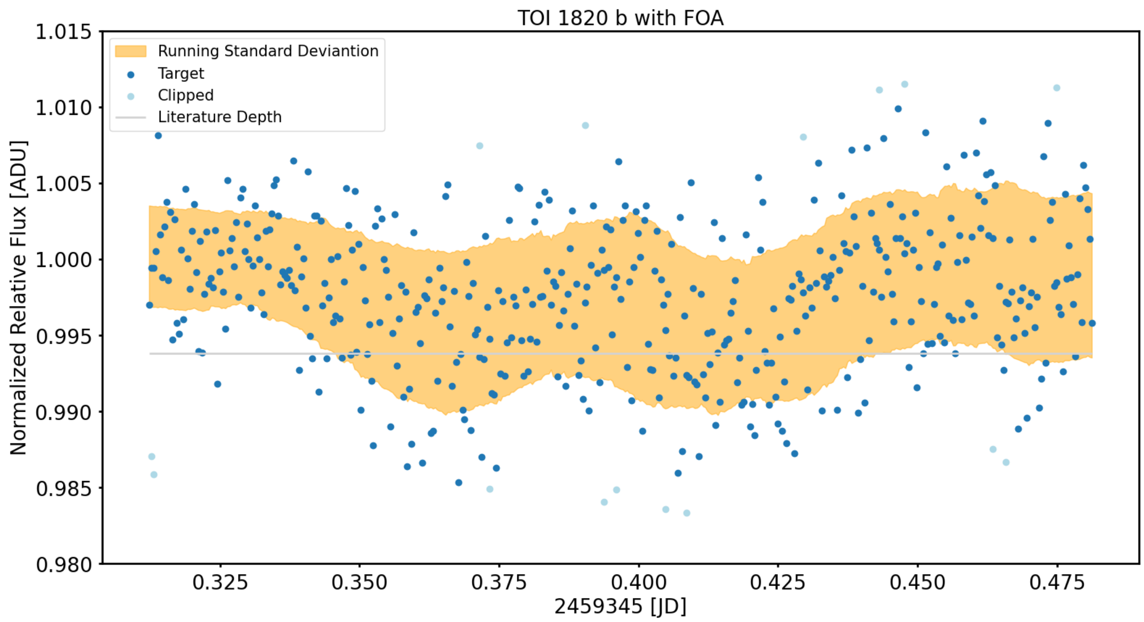

Figure 5.3: The light curve of the full transit of TOI1820 b with Figl. On the x-axis the Julian Date is displayed, and on the y-axis the normalised differential flux is displayed. The observation took place on May 10th 2021 and lasted for 240 minutes. The exposure time was set to 30 s with a target brightness of 11 mag. The entire transit is roughly visible, starting at JD 2459345.325 and ending at JD 2459345.455 with an approximate depth of 0.6%.

To get a better comparison between the two telescopes, I recreated the Nordkuppel light curve of TOI1820 b with the same reference star as from the Figl observation. The light curve is shown in Fig. 5.4 and there is a clear visual difference from the light curve of Nordkuppel with the ten reference stars. The transit is no longer recognisable and the noise level has increased. The median standard deviation decreased to 0.70 % with a range of 0.58 % to 0.89 %, showing the problems that occur when using too faint or an insufficient number of reference stars.
These three light curves from the TOI1820 b observation are fairly different and provide information on the different strengths and weaknesses of the two telescopes. Detailed numbers are presented in Sect. 5.3 and are discussed in Sect. 6.1.

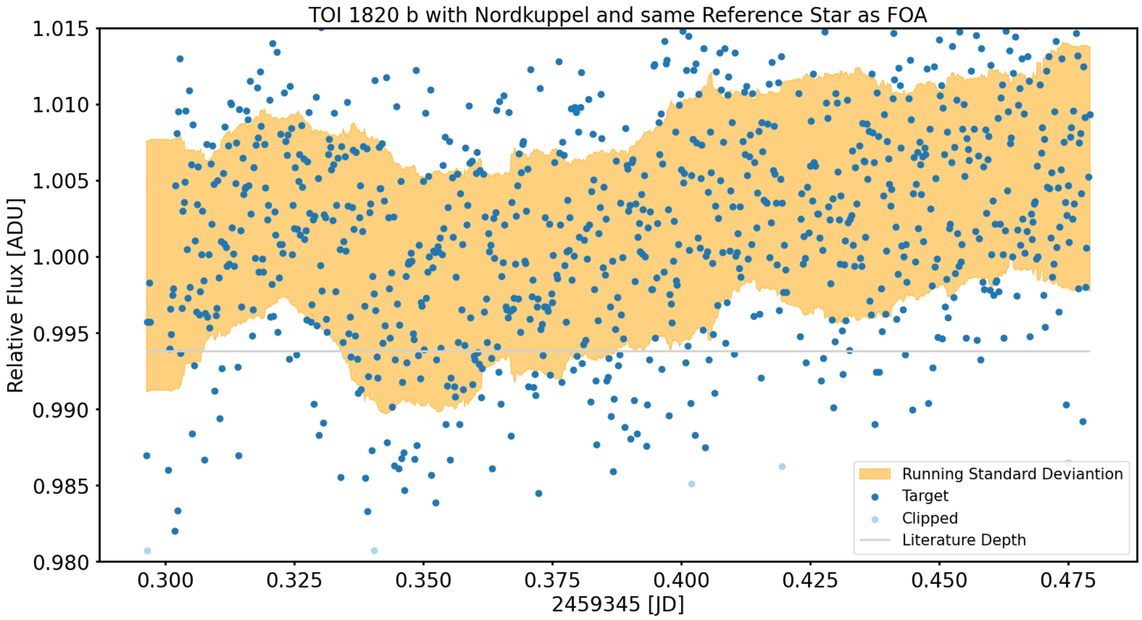

Figure 5.4: The light curve of the full transit of TOI1820 b with Nordkuppel and the same reference star as with the Figl observation. On the x-axis, the Julian Date is displayed, and on the y-axis, the normalised differential flux is displayed. The observation took place on 10 May 2021 and lasted 270 minutes. The exposure time is 15 s with a target brightness of 11 mag. The transit is not visible. It should be from JD 2459345.315 to JD 2459345.455 with an approximately 0.6% depth, but noise dominates this light curve.

5.1.3 HAT-P-36 b

The second transit observed in the dual observation session was HAT-P-36 b. Photometry was also performed with Source Extractor and in Fig. 5.5 the HAT-P-36 b transit light curve with the Nordkuppel telescope is presented. Using ten reference stars, the published depth of 1.59% was relatively well matched to 1.75%. The median standard deviation is 0.44% with a range of 0.29% to 0.51%. The light curve has excellent quality, and the transit is clearly visible. Gradients are not apparent at any time during the observation. Bumps or other inconsistencies, such as those observed for WASP-11 b in Fig. 5.1, are not visible.

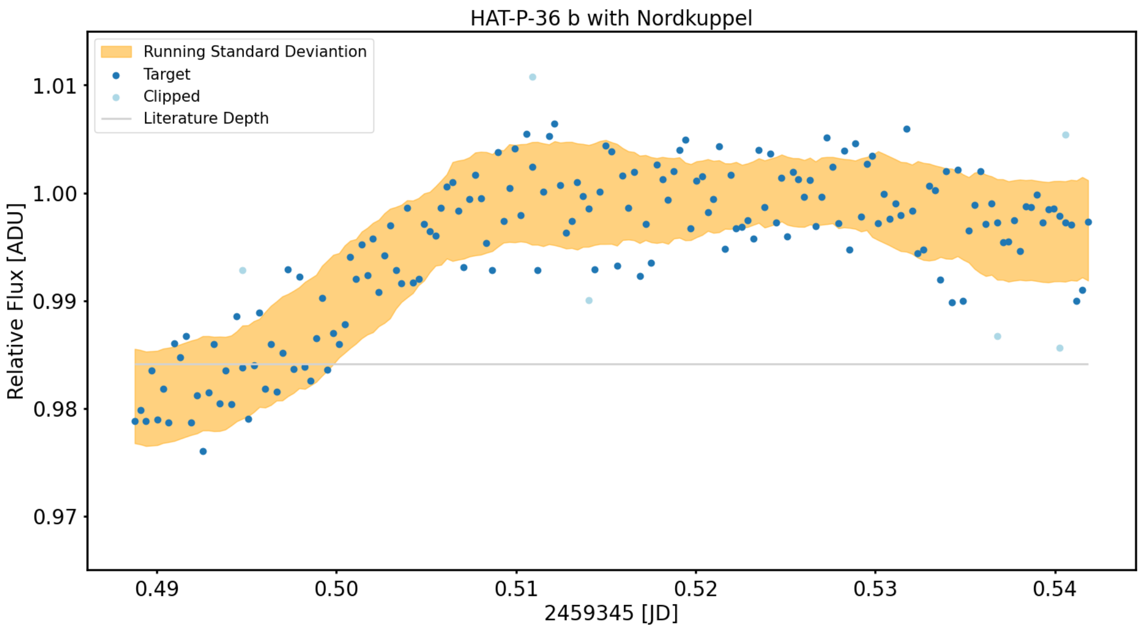

Figure 5.5: The light curve that captures the egress of HAT-P-36 b with Nordkuppel. On the x-axis, the Julian Date is displayed, and on the y-axis, the normalised differential flux is displayed. The observation took place on May 10th 2021 and lasted for 80 minutes. The exposure time is 25 s with a target brightness of 12 mag. The transit is distinctly visible, ending at JD 2459345.505 with an approximately 1.75% depth.

In Fig. 5.6 the Figl light curve of HAT-P-36 b is shown and there are some minor differences from Nordkuppel. The most outstanding characteristic of the Figl light curve is probably that it is, in fact, very similar to the Nordkuppel light curve. The only differences, on the one hand, are the better median standard deviation with 0.42% within a range from 0.25% to 0.51%. However, there is a brightness gradient after the end of the transit for the Figl light curve, leading to a smaller depth of 1.69%. This observation shows very well how important the choice of the reference star is and that the Figl observatory can detect transits if the conditions are right.

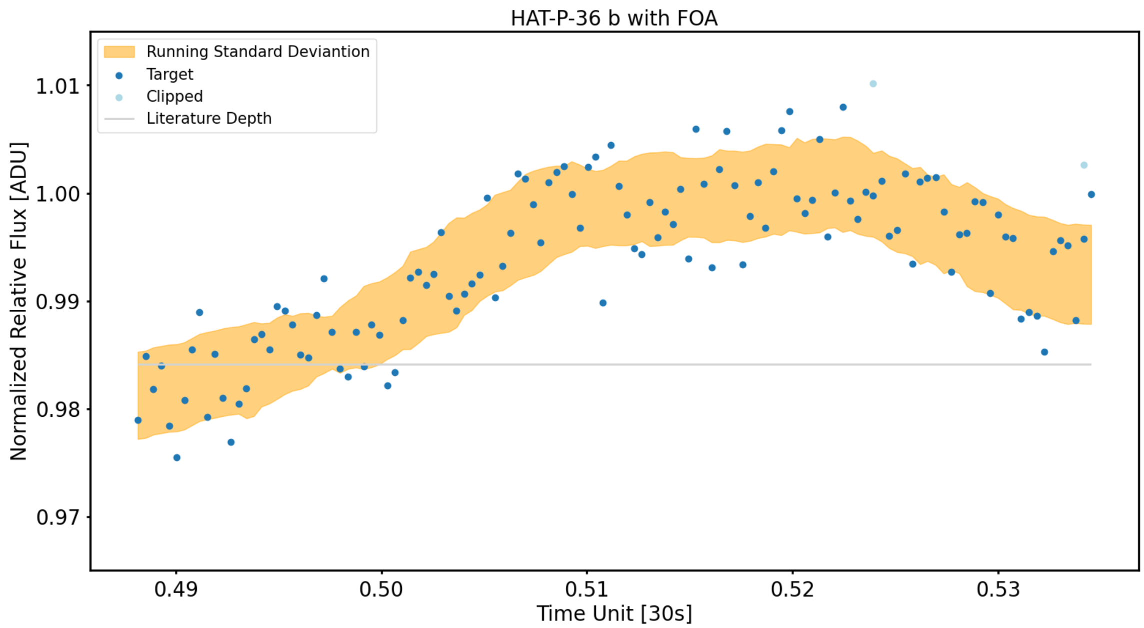

Figure 5.6: The light curve of the egress of HAT-P-36 b with Figl. On the x-axis, the Julian date is displayed, and on the y-axis, the normalised differential flux is displayed. The observation took place on 10 May 2021 and lasted 65 minutes. The exposure time is 30 s with a target brightness of 12 mag. The transit is visible and ends at JD 2459345.510 with a depth of approximately 1.69%.

Similar to TOI1820 b, the Nordkuppel light curve of HAT-P-36 b was recreated with the same reference star as from the Figl observation. This light curve is shown in Fig. 5.7, which shows distinct visual differences compared to the result of Nordkuppel with all ten reference stars. Contrary to the TOI1820 b light curve in Fig. 5.4, the transit is still clearly visible. The transit depth is too deep with 2.5% instead of 1.59% and, at the end, there is a brightness gradient. The median standard deviation is 0.52% within a range of 0.37% to 0.58%, which is more now, but since the depth is deep, the transit is still visible.
These three light curves from the HAT-P-36 b observation are fairly similar and provide good insight into the different strengths and weaknesses of the two telescopes. Detailed numbers are presented in Sect. 5.3 and are discussed in Sect. 6.1.

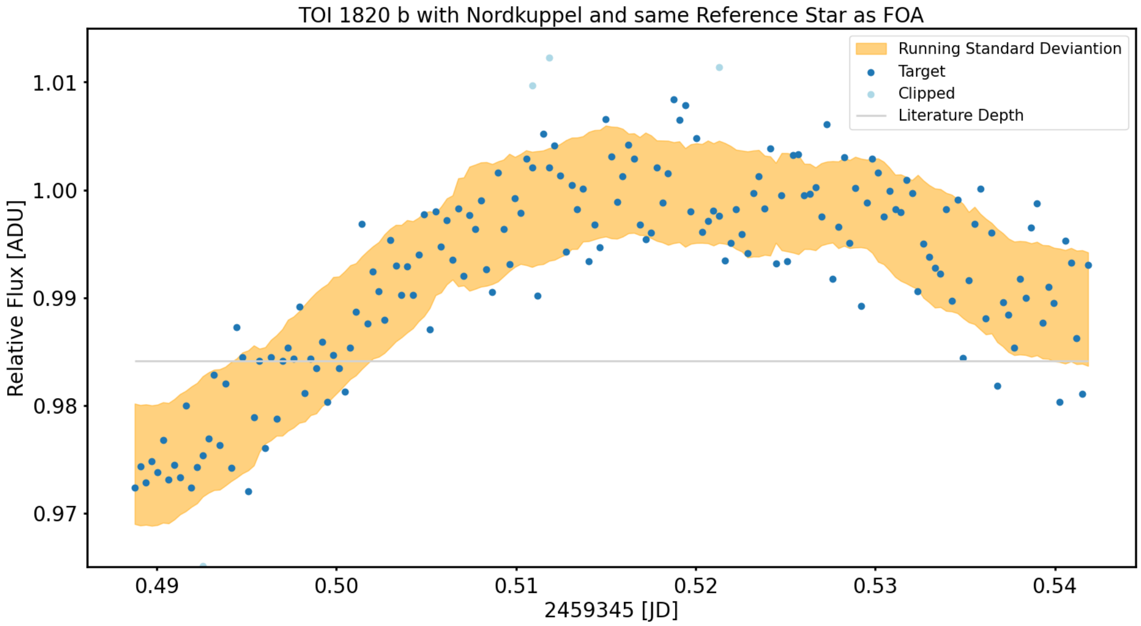

Figure 5.7: The light curve of the full transit of HAT-P-36 b with Nordkuppel and the same reference star as in the Figl observation. On the x-axis, the Julian Date is displayed, and on the y-axis, the normalised differential flux is displayed. The observation took place on 10 May 2021 and lasted for 80 minutes. The exposure time is 25 s with a target brightness of 12 mag. The transit is visible and ends at JD 2459345.515 with approximately 2.5% depth.

5.2 In-Depth Analysis of Light Curves

Looking at the light curves from the previous section, it is apparent that some of them have a brightness gradient that does not originate from the exoplanet transits. There is either a gradient throughout the observation as in Fig. 5.4 or a gradient at a specific part of the light curve as in Fig. 5.2. I will present three phenomena that can explain some of the observed light curve deviations: different spectral types of the used stars, variable stars, and instrumental features.

5.2.1 Atmospheric Extinction

Stars with different temperatures have a different spectral energy distribution (SED) (Planck, 1900). The refraction index depends on the wavelength, and when the light of a star enters the Earth's atmosphere, each wavelength is refracted at an individual angle. Shorter (bluer) wavelengths are refracted stronger than longer (redder) wavelengths (Hansen &

Travis, 1974). This phenomenon might have an impact on the observations of TOI1820 b with the Figl telescope. In this case the reference star was not only 2 mag fainter but also redder, hinting at a different spectral type. The published colour index of the reference star[1], Melotte 111 AV 1957, is BP-RP = 1.1 mag. With the target star being a bluer solar-type star (BP-RP of 0.84 mag), the different spectral types could cause problems when analysing the differential flux. It is expected that the bluer star loses more flux at larger airmass because more light is lost because of the atmosphere. To analyse the intensity of this effect, I developed a rudimentary experiment with synthetic stars of different spectral class that are observed through a refracting atmosphere in the R band.

First, the SED of two stars was simulated by means of a classical Planck black-body function using the following formula:

$$B_\lambda(\lambda, T) = \frac{2hc^2}{\lambda^5} \frac{1}{e^{hc/\lambda k_b T} - 1} \tag{5.1}$$

With $B_\lambda(\lambda, T)$ being black body radiation, λ the wavelength, T the temperature of the star, h the Planck constant, c the speed of light and k_b the Boltzmann constant.

For the extinction coefficient, I started with the values from the Roque de los Muchachos Observatory in La Palma[2]. Since La Palma observatory is located at a higher altitude than Vienna (2400 m vs 250 m) the values were tentatively doubled. In Fig. 5.8 (a), the extinction coefficient is shown as a function of wavelength. Since the values were only available in 10 nm intervals, an interpolation was performed for any other wavelength. The absorption profile of the Bessel R filter was taken from ESO and is presented in Fig. 5.8 (b). For this experiment, I assumed that the observation started at an altitude of 67° and ended at 46°, similar to the actual observations. Using Equ. 5.2, the airmass then ranged from 1.08 to 1.39.

$$X(\zeta) = \frac{\sqrt{(R + H)^2 - (R \cdot sin\zeta)^2} - R \cdot cos\zeta}{H} \tag{5.2}$$

With X being the airmass, ζ the zenith angle, R the Earth radius, and H the scale height.

[1] http://simbad.u-strasbg.fr/simbad/sim-id?Ident=Cl*+Melotte+111+AV+1957
[2] https://www.ing.iac.es/astronomy/observing/manuals/ps/tech_notes/tn031.pdf

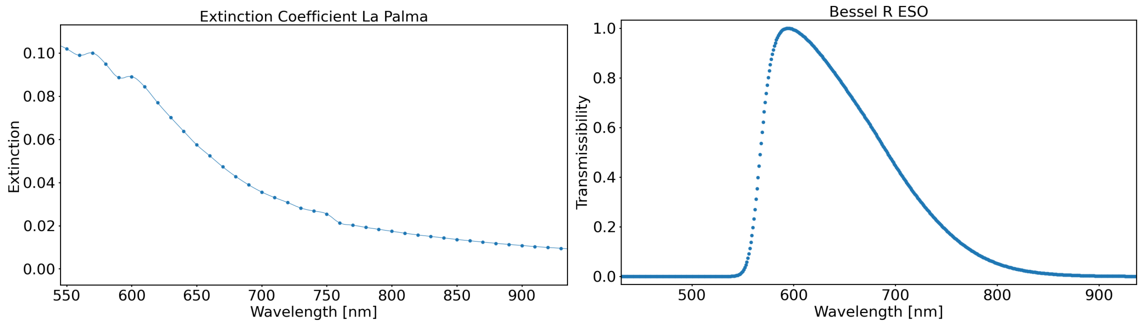

(a) The wavelength-dependent extinction coefficient

(b) The absorption profile of a Bessel R-filter

Figure 5.8: Figure (a) displays the wavelength-dependent atmospheric extinction coefficient of the Roque de los Muchachos Observatory in La Palma. In Fig. (b) the profile of a Bessel R-filter is displayed. The transmission of the filter becomes non-zero at about 550 nm, peaks at around 600 nm, and plummets toward 800 nm.

After gathering all the necessary components, the final flux that reaches the detector can be calculated. To do so, every wavelength of the black-body flux from formula 5.1 was computed with its associated extinction coefficient and filter value 5.8. To combine these parameters, the following formula was used, which is valid for small extinction values.

$$F(T, X) = \int B_\lambda(\lambda, T)\,(1 - A_\lambda \cdot X)\,R_\lambda\,d\lambda, \tag{5.3}$$

with F (T, X) being the final flux depending on the chosen temperature and airmass, $B_\lambda(\lambda, T)$ the assumed black-body radiation of a star depending on the temperature, A_λ the extinction coefficient, X the given airmass and R_λ the transmission of the R filter.

The formula 5.3 presents an estimate of the expected flux values. Figure 5.9 shows the graphs of the reduced black body fluxes with temperatures of 8000 K (black), 6000 K (blue), 5000 K (green), and 4000 K (red) and with an airmass of 1.08 (full line for the beginning of TOI1820 b observation) and 1.39 (dotted line for the end of the TOI1820 b observations). Looking at the diagram, the fluxes still have an intensity distribution similar to that of a black body. After applying the attenuation curve of the R filter and the extinction to the SEDs, the highest intensity wavelengths were similar for all temperatures.
With the final fluxes it is possible to calculate flux proportions, which represent the expected flux losses coming from a change in airmass. For instance, by dividing the two fluxes of the 8000 K star, one with an airmass of 1.39 divided by the one with an airmass of 1.08, it is possible to get the flux loss due to a change in altitude. The different flux losses for the individual stars while they gain airmass are displayed in the following table.

Table 5.1: Overview of how much flux a star with given temperature loses when changing from an airmass of 1.08 to 1.39. Hotter stars lose more flux with more airmass.

Temperature	8000 K	6000 K	5000 K	4000 K
Δ Flux	4.99 %	4.86 %	4.74 %	4.56 %

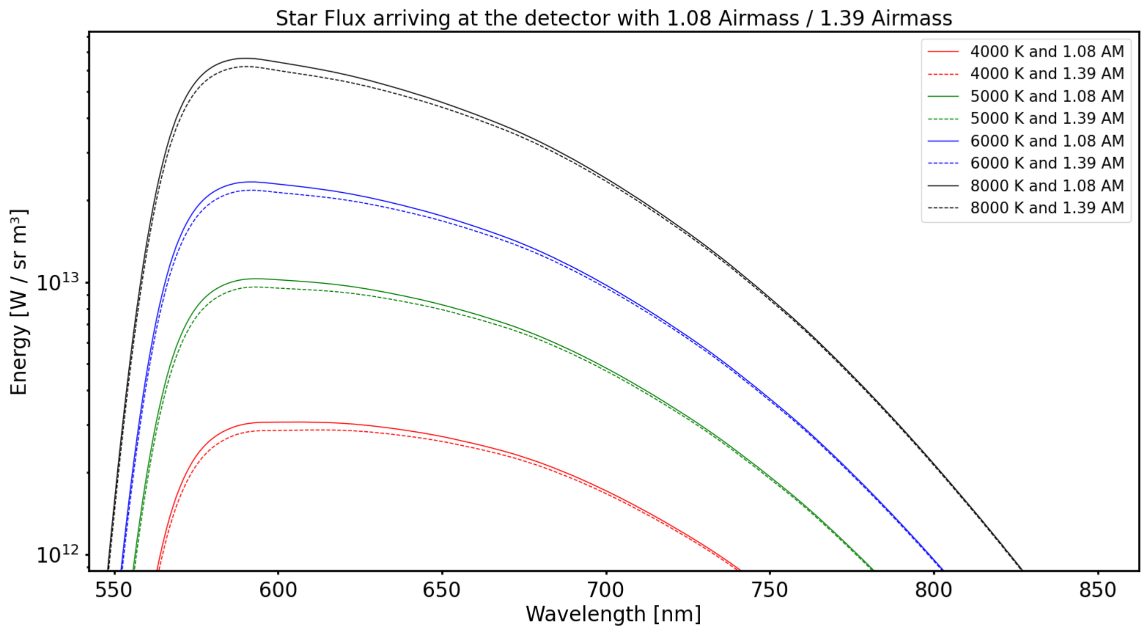

Figure 5.9: The simulated wavelength-dependent flux of a star approximated by black-bodies with temperatures of 4000 K (red), 5000 K (green), 6000 K (blue), and 8000 K (black) at an airmass of 1.08 (solid lines) and 1.39 (dashed lines). On the x-axis, the wavelength is shown and on the y-axis, the logarithmic spectral emissive power, attenuated by an R filter and atmospheric extinction, is displayed.

Table 5.1 shows that all analysed stars lose multiple percentages of flux while changing airmass from 1.08 to 1.39. Hotter stars lose more flux, as can be seen in Tab. 5.1. To obtain an answer on how this phenomenon influences a light curve constructed with differential photometry, I compared the flux ratio of different stars while they changed airmass.

Table 5.2: Overview of how much the differential flux of two stars with given temperatures is lost when changing from an airmass of 1.08 to 1.39. The farther apart the temperatures are, the greater the flux loss between the airmass becomes. 6k/5k is closest to the Figl TOI1820 b observation.

Temperature [K]	8k/6k	8k/5k	8k/4k	6k/5k	6k/4k	5k/4k
Δ Flux	0.14 %	0.26 %	0.46 %	0.12 %	0.31 %	0.19 %

Table 5.2 shows that the expected flux difference from performing differential photometry

with two stars of a different spectral type while the airmass is changing from 1.08 to 1.39, is a few tenths of a percent. For the Figl TOI1820b observation, a flux loss of 0.12 % would be expected. Figure 5.10 shows a zoom-in of the Figl TOI1820 b light curve with an additional orange trend line, which indicates a flux loss over time. When the median of the first 50 data points was compared with the last 100 data points, a flux difference of 0.17 % was discovered, close to 0.12 % from the simulation results. As a consequence, the colour effect might have had an influence on the differential flux and could explain the gradient in this case.

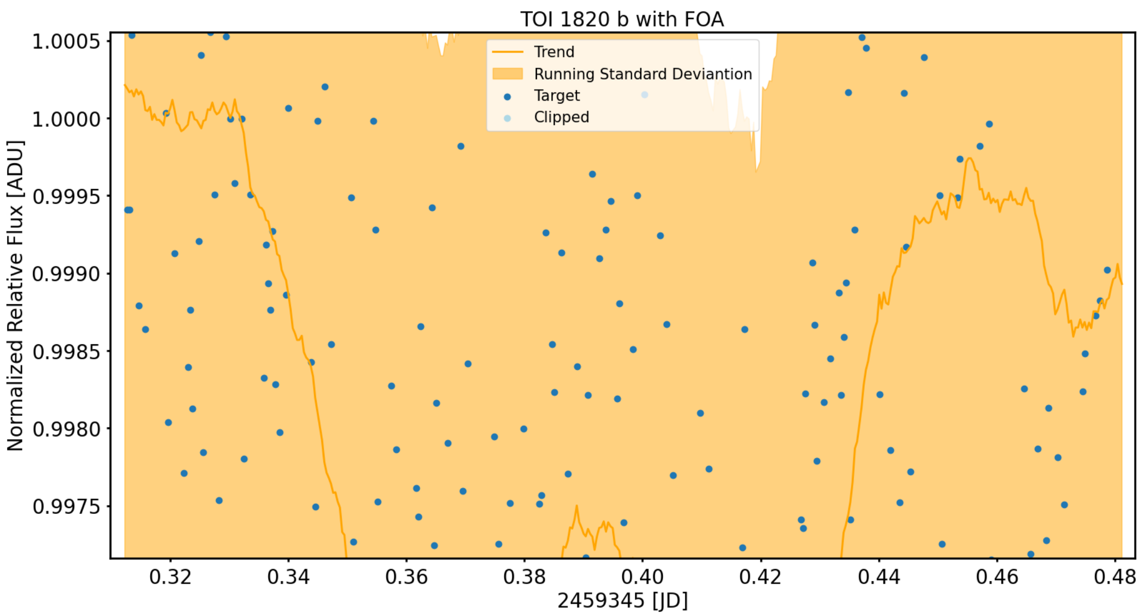

Figure 5.10: Zoom-in on the Figl TOI1820 b light curve with a trend line to visualise the loss in differential flux.

5.2.2 Variable Stars

Another reason for a brightness gradient is an intrinsic change in the flux of a star. There are various reasons for intrinsic variability, and any kind of variable star is a problem for differential photometry. For instance, when a star is old and leaves the main sequence of the HRD, it can become a variable RGB or AGB star (Iben & Renzini, 1983). These stars can exhibit periodic flux changes that occur over a period of multiple hours or days and could explain the variations in the observed light curve. The reference star of TOI1820 b has a Gaia BP-RP colour index of 1.1 which is compatible with typical colours of, oftentimes variable, RGB or AGB stars. In the literature, the following parameters for the reference star of TOI1820 b are available[3]:

Table 5.3: Parameters for the Figl TOI1820 b reference star Melotte 111 AV 1957.

Name	Parallax	m_G	Distance	M_G	$G_{BP} - G_{RP}$
Melotte 111 AV 1957	0.2593 mas	12.9 mag	3857 pc	-0.03 mag	1.1 mag

Given its absolute magnitude and colour index, the star can be placed in the HRD of Gaia, as shown in Fig. 5.11. The reference star is not located on the main sequence but is positioned on the branch of giants. This suggests that the reference star of Figl TOI1820 b could be variable, which could explain the brightness gradient of 0.17 %. The existence of this phenomenon alone is a strong argument for using as many reference stars as possible.

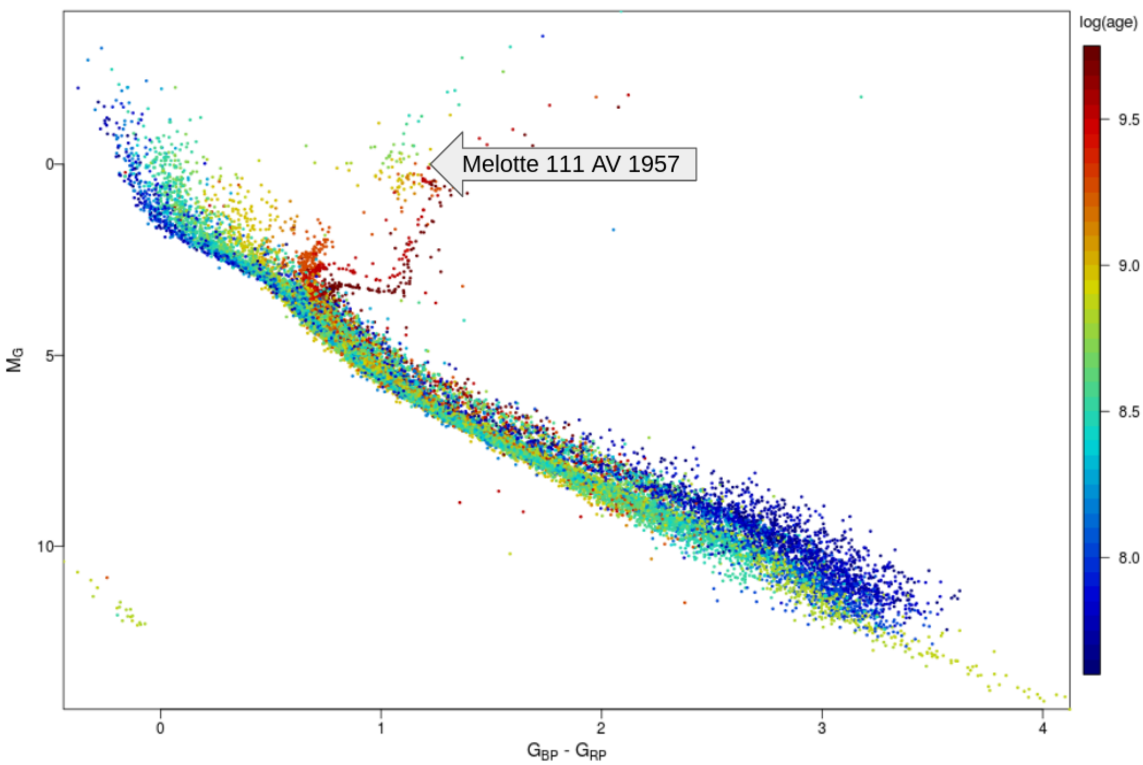

Figure 5.11: The HRD of Gaia DR2 with the highlighted position of the reference star of the Figl TOI1820 b observation. The y-axis shows the absolute magnitude, and the x-axis shows the colour index of the stars. The colours of the scatter points indicate the age of a source.

[3] http://simbad.u-strasbg.fr/simbad/sim-id?Ident=Cl*+Melotte+111+AV+1957

5.2.3 Fixed vs Adaptive Apertures

The last possibility of a brightness gradient that will be discussed are instrumental features. Fig. 5.10 and Fig. 5.4 have the same target and reference star, but their gradients have an opposite direction. This suggests that the instrumental signature was not completely removed during processing.

The methods used also influence the quality of the data and can introduce some method-specific errors. An example is the deviation between the light curves of the TOI1820 b observation with different aperture size determination methods for differential photometry. Figure 5.12 (a) shows the observation with fixed-size apertures, and there are some distinctions to the light curve with apertures with adaptive sizes (b). The most prominent difference is the gradient of the entire light curve when using static apertures. For both light curves, Source Extractor was used, which rules out the possibility of a different approach between two distinct programmes. Therefore, the error leading to the massive brightness gradient should come from using fixed-size apertures. This is a good example of why adaptive-sized apertures are preferred among astronomers.

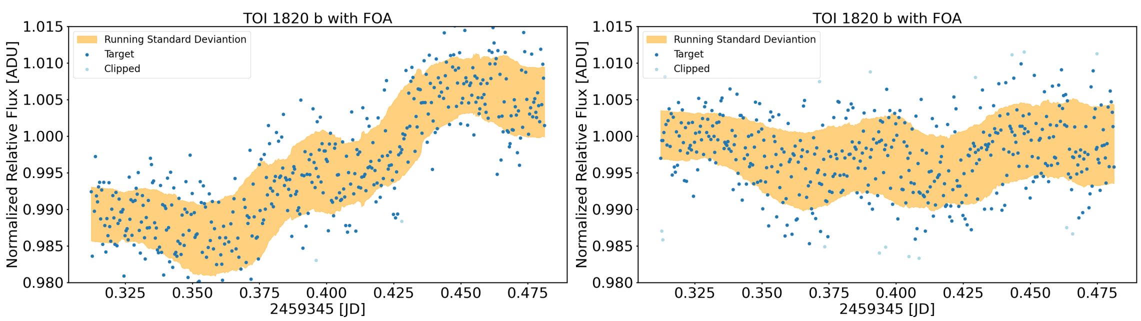

(a) Figl TOI1820 b with static apertures

(b) Figl TOI1820 b with dynamic apertures

Figure 5.12: The light curves of the Figl TOI1820 b observation with fixed apertures (a) and adaptive apertures (b). Although the fixed aperture light curve has a systematic error resulting in a gradient, features, like the bump in the middle, are visible in both observations.

Section 5.2 showed that there can be many reasons for why a light curve has a slight gradient and that it is difficult to identify the exact cause. However, a tiny gradient should not hinder the data analysis process, as long as the gradient is not too steep.

5.3 Statistics

In this section, I review the noise properties of the light curves to evaluate the overall quality of the observations. Table 5.4 lists the measured standard deviations for the simultaneous observations, together with the observation and processing setup.

Table 5.4: Overview of the different dual observation light curves and their standard deviations with their observation-specific setup. The first three rows refer to the TOI1820 b observations, which are Nordkuppel with ten reference stars, Figl with its single reference star, and Nordkuppel with the same reference star as Figl (FRS). The last three rows refer to the HAT-P-36 b observations, in the same order.

Observations	$\overline{Std}$	$\overline{Std_n}$	Time	$\overline{FWHM}$	Aperture
TOI1820 b NK	0.35%	0.31%	15 s	3.94 px / 2.23"	0.8 m
TOI1820 b FOA	0.51%	1.16%	30 s	25.03 px / 2.58"	1.5 m
TOI1820 b NK-FRS	0.70%	0.61%	15 s	3.94 px / 2.23"	0.8 m
HAT-P-36 b NK	0.44%	0.49%	25 s	5.13 px / 2.89"	0.8 m
HAT-P-36 b FOA	0.42%	0.96%	30 s	29.51 px / 2.99"	1.5 m
HAT-P-36 b NK-FRS	0.52%	0.58%	25 s	5.13 px / 2.89"	0.8 m

Before analysing and comparing the standard deviations of the observations, it should be noted that it is not possible to compare the raw measured standard deviations due to different instrumentation. Therefore, I calculated the normalised standard deviations $\overline{Std_n}$ normalised by their exposure time and the aperture area as listed in Tab. 5.4. This allows for a subjective comparison with $\overline{Std}$ and a more objective comparison $\overline{Std_n}$ between the observations. The normalised standard deviations were created by setting the aperture to 1 m and the integration time to 10 s for the six light curves. This leaves the detector (gain) and the number of reference stars as the major remaining differences between the telescopes.

The setup with the lowest noise was achieved by the Nordkuppel observation of TOI1820 b with all ten reference stars with a median standard deviation of 0.35%. The same target observed with Figl and with only one reference star resulted in a worse standard deviation with 0.51%. When using only the single reference star from Figl, the Nordkuppel light curve was dominated by noise with a standard deviation of 0.70%. The normalised setup decreased the standard deviation for the Nordkuppel TOI1820 b observation down to 0.31% with ten reference stars and 0.61% with only one. The normalised standard deviation for the Figl TOI1820 b got worse, up to 1.16%.

Looking at the HAT-P-36 b transit, the Nordkuppel light curve with ten reference stars and the Figl light curve provide a very similar noise level with 0.44% and 0.42% respectively. Only the Nordkuppel light curve with only one reference star is noticeably noisier, but with 0.52% still usable. Contrary to the TOI1820 b observation, the normalised setup increased the standard deviation for the Nordkuppel HAT-P-36 b observation up to 0.49% with ten reference stars and 0.58% with only one. The normalised standard deviation for the Figl HAT-P-36 b also changed, up to 0.96%.

Figure 5.13 shows a plot with the normalised standard deviation over time for a better visual comparison of the different observations. An interesting attribute of the graph is that it shows that the standard deviation of the TOI1820 b FOA observation started really well but got worse over time. The reason could be changing weather conditions. This has a negative influence on the resulting light curve (see Fig. 5.3), which makes the detection quality during this time worse. The other standard deviation trends are relatively stable, except for a short duration of excellent noise quality in the Figl HAT-P-36 b observation.

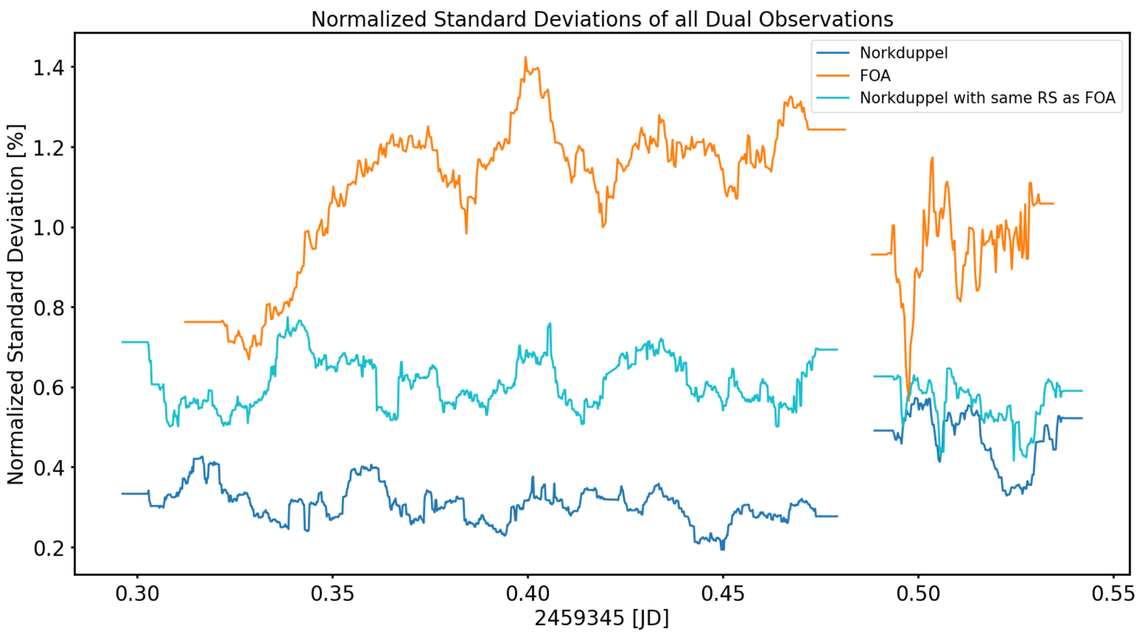

Figure 5.13: Normalised standard deviations of the dual observations over the full time of the observation session. Starting on the left side, TOI1820 b observations are displayed up to JD 2459345.48. Then, after a short break, observations of HAT-P-36 b are shown. Nordkuppel observations with all reference stars are shown in blue, Figl in orange, and Nordkuppel observations with the same reference star as Figl in cyan.

Another factor that can influence the detection quality is the change in the FWHM of sources during the observations (see Fig. 5.14). This can happen due to a change in ambient temperature or a change in weather conditions. The volume of solid objects is directly dependent on their temperature. To some extent, this affects also the telescope's focal length and focus position, which can lead to variable imaging quality (e.g. FWHM) if no adjustments are made. This effect could be seen in Fig. 5.14 with the TOI1820 b FWHM, starting at around JD 2459345.357 as the FWHM starts to increase. Since the Figl FWHM value is increasing faster and has a drop at around JD 2459345.45, this could imply a faster drop in temperature, maybe from a change in weather conditions, which is increasing the seeing and therefore the FWHM additionally. In the standard deviation plot (see Fig. 5.13) and the transit plot (Fig. 5.3) there is also a drop in image quality visible roughly at JD 2459345.4.

Fortunately, variable FWHMs during observations are a manageable problem for photometry. When all the light of an object is captured, regardless of its size, this leads mainly to an increased noise level if the FWHM of the star grows. However, for stable results, it is important to keep the number of pixels of a PSF during an observation as similar as possible. One way to counteract an increase in FWHM caused by a change in temperature would be to refocus on a regular basis. However, most changes in the FWHM of point sources are due to changes in local weather conditions, where, for instance, cirrus clouds can degrade transparency and image quality. As a consequence, it is often more effective to rely on adaptive apertures to compensate for any changes in PSF shapes.

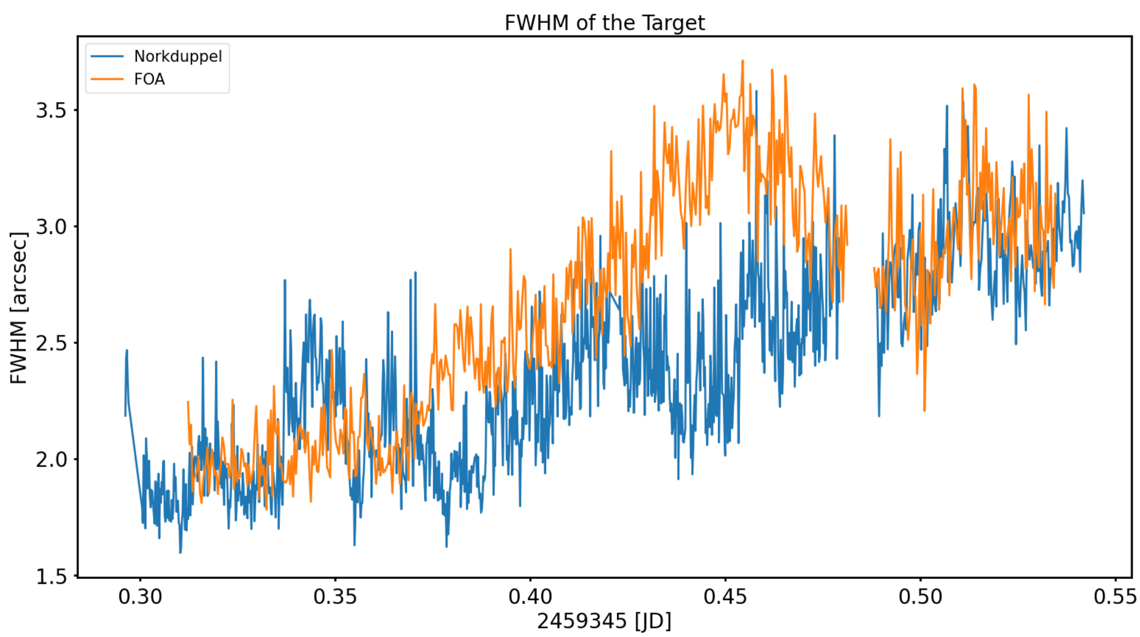

Figure 5.14: FWHM in arcseconds of the targets of the dual observations during the full time of the observing session. Starting on the left side, TOI1820 b is displayed until JD 2459345.48. After a short break, HAT-P-36 b observations can be seen on the right side. Nordkuppel data are shown in blue, and Figl data are shown in orange. The influence of a change in weather and temperature can be read out of such diagrams. This plot suggests changing ambient conditions during observations with the Figl telescope.

To get a better understanding of weather conditions, which can help interpret the standard deviation and FWHM noise, it is possible to look at the background brightness of the images. Clouds reflecting light from surrounding cities brighten the sky. Looking at the average brightness of each image, it is possible to see whether there is more light present, which could result in cloud coverage during the observation. In Figure 5.15, the brightness of the sky over time of each of the two dual observations is presented. The brightness values come from the measured ADU values from the corrected images, normalised by observation-specific parameters such as aperture, integration time, pixel scaling, gain, and quantum efficiency from Tabs. 2.1 and 2.2. At first, the brightness was very high because the observation started at dusk, and it took some time until the sun was low enough not to be influential anymore. What stands out in the plot is that the Nordkuppel background brightness is much higher and contains more potentially disturbing features than the Figl one.

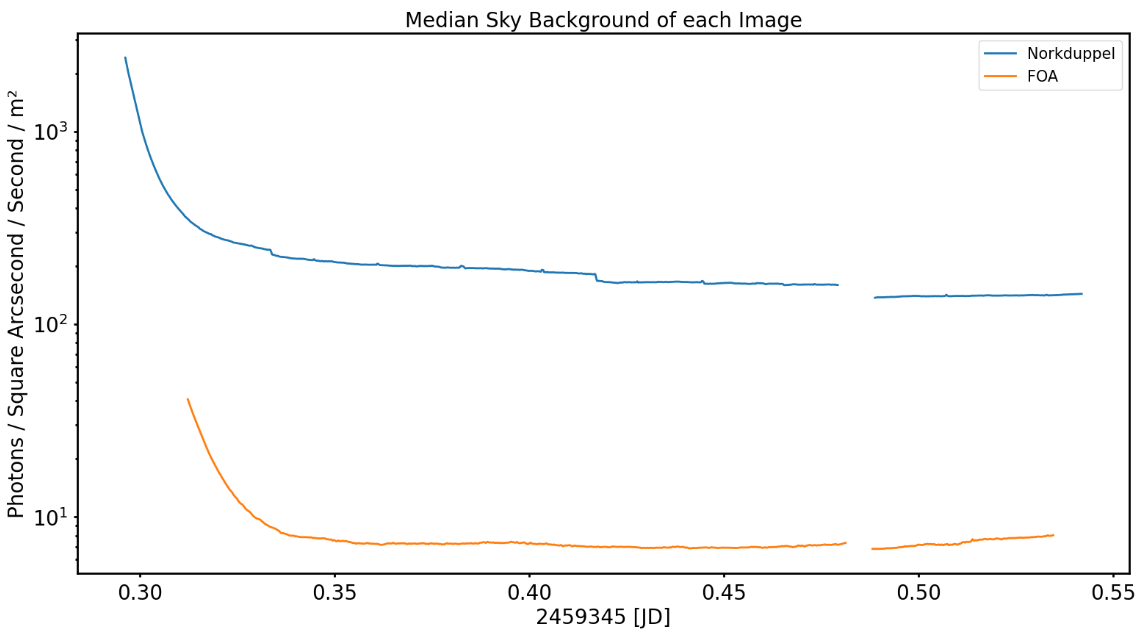

Figure 5.15: Sky background flux as a function of time for the dual observations in photons per square arcsecond per second. Nordkuppel observations are shown in blue, and Figl data are shown in orange. The intensity of light pollution originating from the city of Vienna is clearly visible in the Nordkuppel background, underlining the negative influence of a nearby city on astronomical observations and highlighting the superior geographic location of the Leopold Figl observatory.

Starting with the Figl brightness trend, no visible peaks or gradients are apparent. Only stochastic noise is visible, but it is lower than the Nordkuppel noise. There are no signs of any major clouds or similar phenomena that affect the images. Looking at the Nordkuppel trend, there are many features that can be looked into. The two big steps around JD 2459345.33 and JD 2459345.42 are the two main street lights that dim before midnight in Vienna. Additionally, there is a decline in brightness in the TOI1820 b curve, which is probably a combination of the following phenomena: Even after sunset it takes a few hours to get completely dark, and the telescope is changing its position while following its target. The TOI1820 b observation started with looking to the south and ended with looking to the west. Southwards, the Institute of Astrophysics Vienna is located, whereas westwards the Wienerwald is located, which might explain some of the brightness loss.

The HAT-P-36 b trend curve is fainter and has a slight gradient but is getting brighter. The lower photon amount cannot be explained by the line of sight since the observation started in the west; hence, it might be altitude. The HAT-P-36 b observation started at ten degrees higher altitude than the TOI1820 b was finished, which could lead to less stray light from the streets. Afterwards, the target rapidly sank towards the horizon, collecting more stray light and, therefore, more average background brightness per image.

Another interesting feature of both Nordkuppel observations is small spikes on a regular basis of half an hour. A possible explanation for these spikes could be the nearby train S45 that is passing by. The last feature that will be pointed out is the brightness difference between the two Nordkuppel observations. The rounded median background values are: Nordkuppel TOI1280 b: 195 photons/arcsec$^2/s/m^2$, Nordkuppel HAT-P-36 b: 141 photons/arcsec$^2/s/m^2$, Figl TOI1820 b: 7,2 photons/arcsec$^2/s/m^2$ and Figl HAT-P-36 b: 7,4 photons/arcsec$^2/s/m^2$. There is a flux ratio of 27 for the TOI1820 b observation and a flux ratio of 19 for the HAT-P-36 b observation. When converted to sky brightness units, there is a difference of up to 3.5 magnitudes per arcsec^2. These measurements are very similar to the number of night sky measurements obtained at the Institute of Astrophysics in 2019[4]. The data available from this web resource suggest that the Nordkuppel sky brightness limit is about 19 mag/arcsec^2 while the Figl sky can reach much fainter levels of about 22 mag/arcsec^2. These numbers match well with the values derived from the observations in this thesis.

[4] https://nightsky.univie.ac.at/index.html

5.4 Astrophysical Parameters

In this section, the published and measured astrophysical parameters of the dual observations with their errors are presented. Since no transit was detected at different times and not all exoplanets were observed over the full duration of the transits, some parameters, such as period or inclination, cannot be measured. For that reason, some of the missing parameters were taken from the papers of Knudstrup et al. (2022) and Wang et al. (2019). In this way, the semi-major axis, the planet radius, and the inclination could be calculated. The errors in the required parameters were analysed from the data or again taken from the papers. The propagated errors were calculated using the Gaussian error propagation formula.

$$\sigma_y = \sqrt{\left(\frac{\partial y}{\partial x_1} \cdot \sigma_1\right)^2 + \left(\frac{\partial y}{\partial x_2} \cdot \sigma_2\right)^2 + \left(\frac{\partial y}{\partial x_3} \cdot \sigma_3\right)^2 + \cdots} \tag{5.4}$$

with y being the full equation of a parameter for which errors must be calculated, $x_1, x_2, x_3, ...$ the parameters with known errors in the equation, $\sigma_1, \sigma_2, \sigma_3, ...$ the errors of the parameters, and σ_y the error of the calculated parameter. For calculating the errors of measured values like the transit depth, the standard error of the mean (SEM - in this case with a median, not a mean) was calculated with the following formula.

$$\sigma_{\bar{x}} = \frac{\sigma}{\sqrt{n}} \tag{5.5}$$

with σ being the standard deviation, n the number of data points, and $\sigma_{\bar{x}}$ the SEM. To obtain the error for the transit duration, the following formulas[5] were applied:

$$\sigma_{\tau_{12}} = \sqrt{\left(\frac{t_c}{n_T}\right)^2 + \left(\frac{RMS}{\Delta F\ \tau_{12}}\right)^2} \tag{5.6}$$

$$\sigma_{\tau_{34}} = \sqrt{\left(\frac{t_c}{n_T}\right)^2 + \left(\frac{RMS}{\Delta F\ \tau_{34}}\right)^2} \tag{5.7}$$

$$\sigma_{\tau_{14}} = \sqrt{\sigma_{\tau_{12}}^2 + \sigma_{\tau_{34}}^2} \tag{5.8}$$

With $\sigma_{\tau_{12}}$ being the error of the duration of the ingress, t_c the cadence time of the images, n_T the number of observed full transits (one for TOI1820 b and zero for HAT-P-36 b), RMS is the root mean square for the considered region, ΔF is the depth of the transit, τ_{12}

[5] http://www.telurium.net/PDF/The%20exoplanet%20potential%20from%20single-transit%20detection.pdf

the duration of the ingress, $\sigma_{\tau_{34}}$ the error of the duration of the egress, τ_{34} the duration of the egress and $\sigma_{\tau_{14}}$ the error of the duration of the full transit duration. The errors for stellar parameters such as radius and luminosity were taken from Gaia and included in the error propagation.

Table 5.5: An overview of the astrophysical parameters from the dual observation and from the latest articles Knudstrup et al. (2022), Wang et al. (2019). Combined boxes are used when the value is taken from the literature.

	TOI1820 b			HAT-P-36 b		
Data Set	Nordkuppel	Figl	Literature	Nordkuppel	Figl	Literature
P [days]	4.8607±1e-05			1.327347±3e-06		
ΔF [%]	0.574±2.1e-3	0.303±4.6e-3	0.576±2.0e-4	1.75±0.106	1.69±0.143	1.588±2.9e-4
τ_{14} [min]	168.5±5.9	152.5±10.7	157.92±3.9	133.9±1.07		
a [AU]	0.059±0.018		0.069 ± 5e-03	0.0236±0.0025		0.0238 ± 4e-04
R_P [R_J]	1.109±0.042	0.805±0.031	1.12±0.02	1.449±0.061	1.424±0.073	1.357±0.035
i [deg]	84.37±2.0	84.24±1.96	85.4±0.5	81.41±1.63	81.49±1.63	85.19±0.65
b	0.85±0.16	0.87±0.13	0.79±0.03	0.52±0.08	0.51±0.08	0.373±0.055

Chapter 6

Conclusions

In the final chapter of this thesis, I will draw conclusions on the above-mentioned results and elaborate on their implications. Furthermore, I will make suggestions on how to improve the capabilities for measuring exoplanet transits with the resources available at the University of Vienna.

6.1 Discussion and Evaluation

6.1.1 Light curves

By visually inspecting the transit light curves from the simultaneous observations in Fig. 6.1, already several conclusions can be drawn.

- In the first light curve (a), the full transit of TOI1820 b with Nordkuppel is visible. A total of ten reference stars are used, and the transit is clearly visible. There are no significant gradients or bumps in the light curve, except for the last few measurements, where a minor gradient appears outside of the transit. This light curve excellently visualises the already existing capabilities for measuring transits at the Institute for Astrophysics.
- In light curve (b), the egress of HAT-P-36 b observed with the Nordkuppel is shown. Here, a total of ten reference stars are used. The egress is clearly visible, and the transit depth is about as deep as expected when compared to published values. No significant trends in brightness are visible.
- Continuing with the Figl light curves, panel (c) presents the full transit of TOI1820 b, measured with only one reference star. Although the transit is visible, several differences to the Nordkuppel light curve become apparent. The most significant attribute

is the bump in the middle of the occultation and the larger standard deviation. The end of the light curve is seemingly horizontal but so noisy that the Figl cannot be regarded as the better performing telescope compared to the Nordkuppel. Nevertheless, the transit depth fits well to the results from the literature.

- In light curve (d) the egress of HAT-P-36 b observed with Figl is presented, and again only one reference star is used. This time having only a single reference star was enough for a high-quality light curve because the second star was sufficiently bright and the measured transit depth matches well with published values. In the last parts of the light curve a downward gradient appears. This light curve represents an excellent example of the potential of the Figl telescope with respect to measuring exoplanet transits.

- Panel (e) shows the transit light curve of TOI1820 b using the Nordkuppel with the single reference star that the Figl telescope has access to. Clearly, there is a large difference from the transit measured with ten reference stars in panel (a). The dip is no longer visible, the noise level is higher, and there is even a small upward gradient. It may be argued that the ingress is visible, but even binning the data to reach better signal-to-noise ratios at the expense of cadence would not fully reveal the transit. This light curve showcases the superior light-collecting power of the Figl telescope, since in image (c) the transit was much better visible.

- The last light curve (f) presents the Nordkuppel egress of HAT-P-36 b with only the single reference star from Figl. This time, the transit is still clearly visible, but there are some differences that can be pointed out. Just like in the Figl HAT-P-36 b light curve (d) there is also a brightness drop at the end. Also, the transit depth should be about 2%, here it is nearly 3%. However, the noise level is very similar. This transit demonstrates that not only the instrumentation but additionally the target and reference star selection greatly impact the detection capability of both telescope systems.

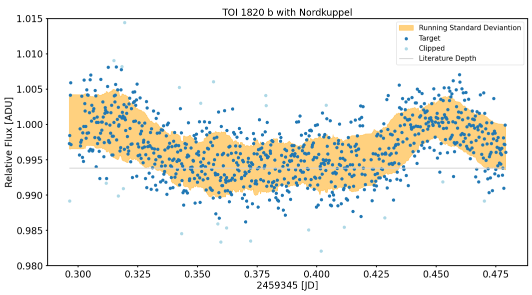

(a) TOI1820 b Nordkuppel

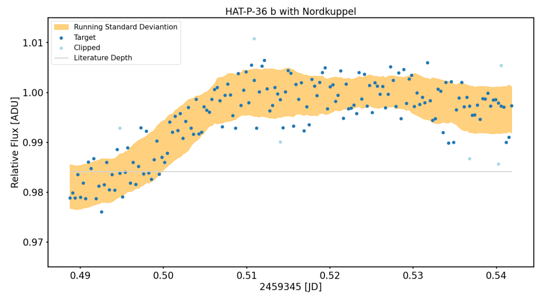

(b) HAT-P-36 b Nordkuppel

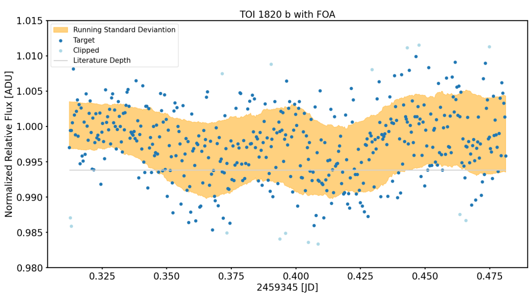

(c) TOI1820 b Figl

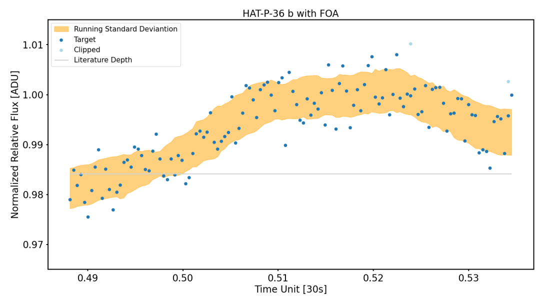

(d) HAT-P-36 b Figl

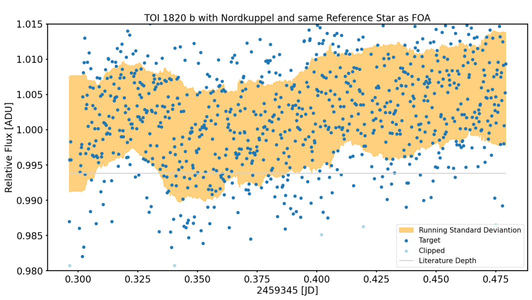

(e) TOI1820 b Nordkuppel 1 RS

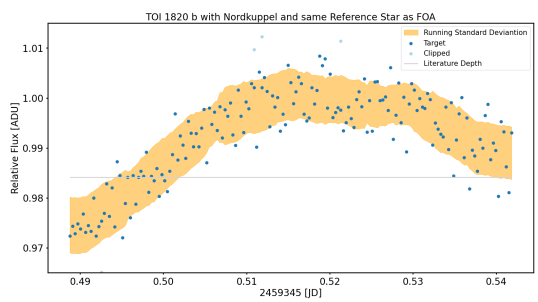

(f) HAT-P-36 b Nordkuppel 1 RS

Figure 6.1: All transit curves from the simultaneous observation. (a) TOI1820 b transit with the Nordkuppel using ten reference stars; (b) HAT-P-36 b egress with the Nordkuppel using ten reference stars; (c) TOI1820 b full transit with the Figl telescope using with the single visible reference star; (d) HAT-P-36 b egress with the Figl using the only available reference star; (e) TOI1820 b full transit with the Nordkuppel using the same reference star as Figl, (f) HAT-P-36 b with the Nordkuppel using the same reference star as Figl.

6.1.2 Noise Characteristics of Light Curves

Analysis of the noise in combination with the detection conditions provided additional information on the noise dependencies. The running standard deviation is displayed in the light curves of Fig. 6.1 as a yellow area. In Tab. 6.1 I again present the standard deviations of the dual observation with additional parameters that influence the noise level.

Table 6.1: The normalised median standard deviations of the six dual observation transit light curves are shown in column two. For a better interpretation of those values, the integration time, the median full wealth half maximum, the telescope aperture, the number of reference stars used, the brightness of the target in the R-band, and the brightness difference range of the used reference star(s) is displayed as well.

Observations_n	$\overline{Std_n}$	Time_n	$\overline{FWHM}$	Aperture_n	RSs	Target RP	RSs ΔRP Range
TOI1820 b NK	0.31%	10 s	3.94 px / 2.23 "	1 m	10	10.48 mag	-0.98 - +3.05 mag
TOI1820 b FOA	1.16%	10 s	25.03 px / 2.58 "	1 m	1	10.48 mag	+2.16 mag
TOI1820 b NK-FRS	0.61%	10 s	3.94 px / 2.23 "	1 m	1	10.48 mag	+2.16 mag
HAT-P-36 b NK	0.49%	10 s	5.13 px / 2.89 "	1 m	10	11.58 mag	-1.62 - +2.21 mag
HAT-P-36 b FOA	0.96%	10 s	29.51 px / 2.99 "	1 m	1	11.58 mag	-0.35 mag
HAT-P-36 b NK-FRS	0.58%	10 s	5.13 px / 2.89 "	1 m	1	11.58 mag	-0.35 mag

A normalisation with respect to aperture area and exposure time enables additional insight into the detection capabilities of the telescopes and their instruments. Before evaluating the normalised standard deviation, I briefly summarise the influence of the observation-specific parameters in Tab. 6.1.

- Exposure time: Longer integration time leads to higher S/N in individual exposures, but requires more reliable telescope tracking. A shorter integration time is useful for better time resolution of the light curve. Due to the normalisation with aperture area and exposure time, for all observations the standard deviation increased.
- $\overline{FWHM}$: Using more pixels picks up more read-out noise and dark current. These types of noise need to be investigated and compared to obtain a better evaluation of their influence on the quality of the observations. Detailed values are listed in Tab. 6.2.
- Aperture: A larger aperture leads to more photons collected, and hence a higher S/N at a given exposure time. In this case, the normalised standard deviation of the Nordkuppel data decreased and the standard deviation of the Figl observations increased because of normalising the aperture diameter to 1m.
- Reference stars (RSs): Using multiple reference stars decreases the amount of noise that is propagated into the final light curve. Both observations with ten reference stars have a lower standard deviation than those with only a single reference star.

- Target brightness (measured in the Gaia RP band; target RP): Brighter targets require less integration time. While observing stars in a magnitude range of about 10 - 15 mag, fainter targets offer more reference stars.
- RSs ΔRP Range: Faint reference stars have a low S/N and contribute more noise to the light curve.

Only observations with similar setups can be compared. This applies to the observations of TOI1820 b and HAT-P-36 b when the same reference star is used for differential photometry.

For the TOI1820 b transits with a single reference star, the Figl telescope has a higher normalised standard deviation of 1.16% compared to the Nordkuppel with only 0.61%. The same can be seen at the HAT-P-36 b transits with a single reference star. Figl has a normalised standard deviation of 0.96%, while the data from the Nordkuppel have 0.58%. This suggests that with the same aperture and integration time, the Nordkuppel setup offers superior detection quality. With the same target, reference star, and observation setup, the only differences left are the location (background), the detector (gain), and optical elements in the telescope and instrument. The different background values in Fig. 5.15 and the different $\overline{FWHM}$ values in Tab. 6.1 motivate an analysis of the signal-to-noise ratio. The signal-to-noise ratio can be obtained with

$$\frac{S}{N} = \frac{N_*}{\sqrt{N_* + n_{pix}(N_{BG} + N_D + N_R{}^2)}}, \tag{6.1}$$

with $\frac{S}{N}$ being the signal-to-noise ratio, N_* the amount of photons collected (or equivalently electrons) from the object, n_{pix} the number of pixels, N_{BG} the background flux, N_D the dark current, and N_R the read-out noise per pixel. The S/N values of the four dual observations are presented in Tab. 6.2. For a more reliable comparison, all values are normalised to an aperture of 1 m and an integration time of 10 s.

Table 6.2: Normalised S/N values of the dual observation and applied parameters. The dark current N_D was not considered due to its negligible influence for both detectors.

Observations	S/N	N_*	n_{pix}	N_{BG}	N_R
TOI1820 b NK	820.5	681352 e-	12.2 px	343.7 e-/px	18.1 e-/px
TOI1820 b FOA	586.3	345855 e-	492.1 px	0.7 e-/px	1.5 e-/px
HAT-P-36 b NK	477.2	239045 e-	20.7 px	247.9 e-/px	18.1 e-/px
HAT-P-36 b FOA	358.7	130657 e-	684.1 px	0.7 e-/px	1.5 e-/px

Table 6.2 shows that the normalised S/N values of Figl are, in fact, lower than their comparable Nordkuppel values. In the case of the TOI1820 b observation, the Nordkuppel

normalised S/N is 1.7 times better and for the HAT-P-36 b observation, the difference is a factor of 1.6. These values are close to the ratios of the normalised standard deviations, indicating that the measured signal-to-noise ratio is already an excellent indicator for the noise properties of the light curves. For the TOI1820 b observation, the Nordkuppel normalised standard deviation is 1.90 times better, and for the HAT-P-36 b observation the difference is a factor of 1.65. For the HAT-P-36 b observation the ratios match nearly perfectly and for the TOI1820 b observation there is a small gap of 10%, which confirms the results from Tab. 6.1. The lower flux received on the detector from the Figl telescope should be the reason for the S/N being smaller than expected for the Figl targets. The cause of this flux loss might be related to the larger number of optical elements used for the Figl telescope, in particular a non-removable polarisation filter in the optical path.

This leads to the conclusion that the current instrumental setup of Figl is outperformed in many cases by the smaller Nordkuppel telescope. Another factor to consider is the pixel scale of the detectors. While the Nordkuppel setup projects the PSF FWHM of sources onto about 4 pixels, the Figl setup spreads the received light over a much larger area (typically with an FWHM of 25 pixels). Hence, the light received with the Figl setup is distributed on an area 40 times larger when compared to the Nordkuppel. As a consequence, also the total read-out noise level is elevated, negatively impacting the signal-to-noise ratios. One solution for this issue would be on-chip binning to reduce the total read-out noise.

6.1.3 Astrophysical Parameters

The goal of many follow-up observations of exoplanet transits is to determine the astrophysical parameters of the star-planet system. In the following paragraphs, the results from Tab. 5.5 will be discussed.

Starting with the parameters obtained for TOI1820 b, the orbital period P of 4.8607±1e-05 days was taken from the work of Knudstrup et al. (2022), because only one transit was observed with both telescopes. Since at least two transits are required to calculate the orbital period of the system, this parameter could not be derived using only the data presented in this thesis. The transit depths Δ F were determined to be 0.574±2.1e-3 and 0.303±4.6e-3 percent. The Nordkuppel value matched the paper value of 0.576±2.e-4 very well. The value of the Figl telescope could not be reliably measured due to the prominent bump in the light curve. The transit duration τ_{14} was derived to be 168.5±5.9 minutes and 152.5±10.7 minutes, relatively close to the published value of 157.92±39 minutes. Since the orbital periods are the same for the Nordkuppel and Figl observations and they orbit the same star, the semi-major axis was calculated with 0.059±0.018 au for both. The difference in the published value could be explained by assuming different values for the mass. The radius R_P of the exoplanet also varies for the two observations.

Nordkuppel's value of 1.109±0.042 R_J is close to the published value of 1.12±0.02 R_J. In contrast, the value obtained from the Figl data, 0.805±0.031 R_J is not compatible with the reference value within the measured erros. The inclination i and the impact parameter b show realistic values, although with large errors.

Next, the parameters of HAT-P-36 b are discussed. This time, not only was the period P of 1.327347±3e-06 days, but also the duration of 133.9±1.07 minutes taken from the work of Wang et al. (2019). Since only the egress of the transit was observed, I was unable to determine its full duration. The only parameter that could be calculated was the transit depth ΔF with 1.75±0.106 and 1.69±0.143, both slightly larger than the published value of 1.588±2.9e-4. The large errors are the result of the few data points available from the observations. For the semi-major axis the values for the Nordkuppel and Figl telescopes were again identical due to the same orbital period. I obtained 0.0236±0.0025 au from the observations, compared to the published value of 0.0238±4e-04. With a greater depth, the planet radii R_P were also larger. From my observations, I calculated 1.449±0.061 and 1.424±0.073, compared to the published value of 1.357±0.035 R_J. For the impact parameter b and the inclination i, I calculated 81.41±1.63 and 81.49±1.63 compared to 85.19±0.65 degrees for the inclination. Since only the egress was detected, some parameters were taken from previous publications, and some parameters were calculated with a small number of data points.

The calculated astrophysical parameters for the exoplanets match well with the published values. The main error sources for the determined values were the stellar mass (brightness) and stellar radius, both taken from the Gaia catalogue (Gaia Collaboration et al., 2016) which can explain the differences from the published values and the error budget.

6.1.4 Summary

The main conclusions of this thesis are as follows.

- Planning observations of exoplanet transits is time-critical and requires thorough preparations. Weather and ambient temperature must be monitored during observations to help interpret visible gradients or other inconsistencies in the constructed light curves.
- The number of reference stars that are used for differential photometry has a strong impact on the quality of the produced light curves. If only a few reference stars are available, they need to be of similar brightness (or brighter) to the target and ideally have a similar spectral type. If these conditions are met, even with a single well-matching reference star, high-quality light curves are obtainable.
- Careful use of flux measurement tools and methods to construct light curves is critical to obtain optimal results. Furthermore, measuring fluxes with adaptive-sized apertures leads to more stable results compared to fixed-size apertures.
- The sky background brightness is up to 27 times brighter at the Institute of Astrophysics in Vienna compared to the night sky at the Figl observatory. This has major implications for the ability to make follow-up observations. Together with the inherently larger aperture, transits of faint targets can only be reliably measured with the Figl telescope.
- The Nordkuppel telescope with its current instrumentation is already well suited for measuring exoplanet transits and follow-up observations. On the contrary, the Figl telescope can only deliver reliable transit measurements if a nearby bright reference star is available. Furthermore, to provide light curves for many currently known follow-up targets that are accessible from the geographic location of the observatory, an upgrade to the instrumentation, specifically an increased field of view, is required.

6.2 Outlook

Looking at current and future exoplanet missions searching for new planets, it is clear that the need for follow-up missions will continue. Table 6.3 gives an overview of current and future planet-hunting missions.

Table 6.3: Current and future Space Missions for exoplanet discovery and analysis. Most of them have yet to discover exoplanets, but for some an estimated amount of observed exoplanets can be quoted.

Ongoing Missions	**Number of Exoplantes**	**Date**	**Method**
Gaia (DR4)	0 (10000)	2013 - present	Astrometry
TESS	233+	2018 - present	Transit Method
CHEOPS	2+	2019 - present	Transit Method
JWST	0	2021 - present	Transit Method / Radial Velocity / Atmosphere
Planned Missions			
ARIEL	0 (1000)	2029 - 2033	Transit Method / Atmosphere
PLATO	0	2026 - 2032	Transit Method
RST	0 (2.500)	2025 - 2031	Direct Imaging / Micro Lensing
TOLIMAN	0	2023 - 2026	Astrometry
Twinkle	0 (700)	2024-2031+	Atmosphere

Acronyms: Transiting Exoplanet Survey Satellite (TESS Ricker et al., 2015), James Webb Space Telescope (JWST Gardner et al., 2006), Atmospheric Remote-sensing Infrared Exoplanet Large-survey (ARIEL Tinetti et al., 2018), PLAnetary Transits and Oscillations of stars (PLATO Rauer et al., 2014), Roman Space Telescope (RST Green et al., 2012), Telescope for Orbit Locus Interferometric Monitoring of our Astronomical Neighbourhood (TOLIMAN Tuthill et al., 2018).

It should be noted that the exoplanet missions of Tab. 6.3 contain missions not only to find exoplanets, but additionally to analyse them in more detail. The column 'Method' contains a reference to 'Atmosphere', which means that the atmospheric components of the exoplanets will be measured with a spectrometer. CHEOPS or ARIEL will focus on characterising existing exoplanets in more detail, while missions like TESS or PLATO are designed to find as many new exoplanets as possible. Any of the mentioned space missions can send out alerts, and it is the function of the follow-up community to identify the signal as a false-positive or confirm the target as an exoplanet.

To give an example of how my work can continue, the latest TESS exoplanet follow-up programme was analysed. To obtain the number of future observation possibilities, I investigated the currently known 5845 TESS Objects of Interest (TOIs) listed on the MIT website[1]. First, I checked which objects are visible from the geographic location of the observatories. To this end, the ephemeris of the Sun and the TOIs were checked, and the dates when the altitude of the TOIs was above 40 degrees and the Sun was six degrees below the horizon were calculated. As the final criterion for suitable candidates, objects were required to be observable for at least 5 % of the year (corresponding to about 200 hours). This leads to a total of 2815 TOIs that are observable from Vienna throughout the year.

To compare the telescopes, I analysed how many of the TOIs can be observed with the Nordkuppel or Figl telescopes, also providing at least one, five, or ten reference stars. The brightness of the reference stars was filtered using the Gaia RP band with a maximum brightness difference of two magnitudes between the TOI and its reference stars. For a field of view of 18' x 18' for the Nordkuppel and 3' in diameter for the Figl, the results of this analysis are shown in Fig. 6.2. Requiring at least a single reference star, the Nordkuppel can observe virtually every TOI currently listed, while the Figl can observe about half of them. With five or more reference stars, differential photometry can be substantially improved. With this setup, there are still more than 80 % of the TOIs available for Nordkuppel observations. On the other hand, the number of Figl TOIs with five or more reference stars dropped to about 10 %. With ten or more reference stars with a brightness similar to that of the target star, the quality of the differential photometry is expected to be outstanding. This applies to nearly two-thirds of all TOIs when using the Nordkuppel telescope and only 3% when using the Figl telescope. These 3% (corresponding to 95 TOIs) appear to be a large number, given the small field of view. After looking into individual TOIs, two factors allow one to have ten reference stars for the Figl. First, targets in the plane of the Milky Way naturally have many neighbouring stars because of the significantly increased stellar density. Second, there are substantially more stars with fainter magnitudes that are still observable with Figl. Although the median brightness for all TOIs is 11.5 mag, there are some sources with magnitudes of 16 or less. All of the 95 TOIs of the ten plus reference star Figl selection belong to one or both of these categories.

[1] https://tev.mit.edu/data/

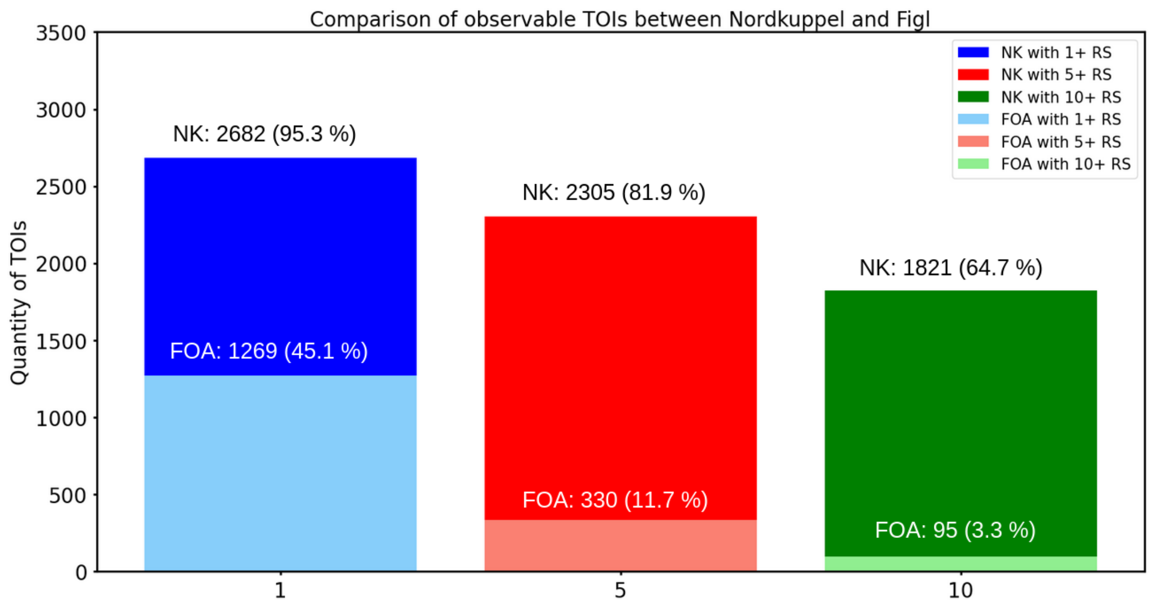

Figure 6.2: This diagram shows how many TOIs can be detected with the Nordkuppel and Figl telescopes with different minimum amounts of reference stars. On the y-axis, the amount of observable TOIs is shown, and on the x-axis, the amount of minimum reference stars is shown. For the Nordkuppel and Figl values, the bars overlap to get a better visual comparison percentage-wise. On top of each bar is the ratio of detectable TOIs to the total of observable TOIs for Vienna.

6.3 Suggestions for Local Infrastructure

To conclude this thesis, several improvements to the existing telescope infrastructure can lead to better efficiency for follow-up observations of exoplanet transits at the University of Vienna. First, hardware modifications for the Figl and second, telescope maintenance and support. The Nordkuppel telescope already performs well with its current CCD camera. It offers a sufficiently large field of view, and its location in the city and its aperture size make it very efficient for studying transits of bright targets. The Figl, on the other hand, could be improved with several upgrades. Looking at the technical specifications[2], the RC focus, which was used for this thesis, potentially can provide a field of view of $1°x1°$. Exploiting this option, the Figl, with its 1.5 m aperture, would easily outperform the Nordkuppel, particularly for fainter objects. To reach this potential, the Figl telescope would need to be refitted with a new camera. With the currently deployed CCD camera, for instance, a field of view of 10' x 10' is achievable via refitting. Another option would be to obtain a new full-frame CCD or a camera specifically built for the purpose of measuring exoplanet

[2] https://foa.univie.ac.at/instrumentation/15m-teleskop/

transits to use an even larger field of view. The flange used to mount Figl's cameras is similar to instruments operated by ESO (OEFOSC which is similar to DFOSC[3]), which could facilitate a uniform assembly mechanism.

This leads to the second important aspect, regarding the maintenance of the entire telescope infrastructure. Since the workshop at the Institute of Astrophysics was closed, there is no more dedicated staff to maintain the telescopes. However, to successfully operate facilities of such scales (particularly the Figl telescope), dedicated and continuous technical support is critical. As a consequence, often the know-how and the required effort to maintain the telescopes is pushed towards scientific personnel. A specialist who is responsible for the safety and the proper functionality of the Figl and Nordkuppel telescopes would be a huge relief for scientists and students and would dramatically improve the efficiency of the observatories.

6.4 Acknowledgements

I want to thank my supervisor, Dr. Stefan Meingast, for overseeing my work process and always supporting me with advice in times of need. He made sure that my work had the necessary depth and scientific methods for a successful master thesis. I also want to thank AO Prof. Werner Zeilinger and Dr. Günther Wuchterl for their additional input of scientific knowledge concerning instrumentation and exoplanets. My colleagues supported me as well in case I got stuck on a coding problem or when I needed a philosophical discussion on a specific topic. The Astronomy community is awesome! Last but not least, my parents also supported me by their regular reality checks and by making sure that I could focus on my work. Therefore, I am very grateful to anyone who helped and supported me during the time I worked on my master thesis.

[3] https://www.eso.org/public/austria/teles-instr/lasilla/danish154/dfosc/

Bibliography

Agol E., Cowan N. B., Knutson H. A., Deming D., Steffen J. H., Henry G. W., Charbonneau D., 2010, ApJ, 721, 1861

Alam S., et al., 2015, ApJS, 219, 12

Astropy Collaboration et al., 2013, A&A, 558, A33

Baglin A., et al., 2006, in 36th COSPAR Scientific Assembly. p. 3749

Bakos G., Noyes R. W., Kovács G., Stanek K. Z., Sasselov D. D., Domsa I., 2004, PASP, 116, 266

Bakos G. Á., et al., 2010, ApJ, 710, 1724

Bakos G. Á., et al., 2012, AJ, 144, 19

Bertin E., Arnouts S., 1996, A&AS, 117, 393

Borucki W. J., et al., 2009, Science, 325, 709

Bouma L. G., et al., 2020, AJ, 160, 239

Bradley L., et al., 2020, astropy/photutils: 1.0.0, Zenodo, doi:10.5281/zenodo.4044744

Clarkson W., et al., 2008, ApJ, 684, 1110

Dravins D., Lindegren L., Mezey E., Young A. T., 1998, PASP, 110, 610

Gaia Collaboration et al., 2016, A&A, 595, A1

Gaia Collaboration et al., 2018, A&A, 616, A10

Galiazzo M. A., Zeilinger W. W., 2013, Journal of the Association of Lunar and Planetary Observers, the Strolling Astronomer, 55, 17

Gardner J. P., et al., 2006, Space Sci. Rev., 123, 485

Ginsburg A., et al., 2019, AJ, 157, 98

Green J., et al., 2012, arXiv e-prints, p. arXiv:1208.4012

Groenewegen M. A. T., 2004, A&A, 425, 595

Handler G., Meingast S., 2011, A&A, 533, A70

Hansen J. E., Travis L. D., 1974, Space Sci. Rev., 16, 527

Howell S. B., Everett M. E., Sherry W., Horch E., Ciardi D. R., 2011, AJ, 142, 19

Howell S. B., et al., 2014, PASP, 126, 398

Huang C. X., et al., 2020, Research Notes of the American Astronomical Society, 4, 204

Hunter J. D., 2007, Computing in Science and Engineering, 9, 90

Iben I. J., Renzini A., 1983, ARA&A, 21, 271

Jehin E., et al., 2011, The Messenger, 145, 2

Jontof-Hutter D., et al., 2016, ApJ, 820, 39

Kepler J., 1619, Ioannis Keppleri harmonices mundi libri V : quorum primus harmonicus ... quartus metaphysicus, psychologicus et astrologicus geometricus ... secundus architectonicus ... tertius proprie ... quintus astronomicus & metaphysicus ... : appendix habet comparationem huius operis cum harmonices Cl. Ptolemaei libro III cumque Roberti de Fluctibus ... speculationibus harmonicis, operi de macrocosmo & microcosmo insertis. Johann Planck, doi:10.3931/e-rara-8723

Knudstrup E., et al., 2022, arXiv e-prints, p. arXiv:2204.13956

Kuiper G. P., 1938, ApJ, 88, 472

Lendl M., et al., 2020, A&A, 643, A94

Luis R., Tusnski Valio A., 2011, The Astrophysical Journal, 743, 97

Mancini L., et al., 2014, A&A, 568, A127

Marcy G., Butler R. P., Fischer D., Vogt S., Wright J. T., Tinney C. G., Jones H. R. A., 2005, Progress of Theoretical Physics Supplement, 158, 24–42

Marois C., Macintosh B., Barman T., Zuckerman B., Song I., Patience J., Lafrenière D., Doyon R., 2008, Science, 322, 1348

Mayor M., et al., 2003, The Messenger, 114, 20

Morton T. D., 2012, ApJ, 761, 6

Patat F., Ugolnikov O. S., Postylyakov O. V., 2006, A&A, 455, 385

Pedregosa F., et al., 2012, arXiv e-prints, p. arXiv:1201.0490

Penny M. T., Gaudi B. S., Kerins E., Rattenbury N. J., Mao S., Robin A. C., Calchi Novati S., 2019, ApJS, 241, 3

Pepper J., et al., 2007, PASP, 119, 923

Perryman M., Hartman J., Bakos G. Á., Lindegren L., 2014, ApJ, 797, 14

Planck M., 1900, Zur Theorie des Gesetzes der Energieverteilung im Normalspectrum; von M. Planck. Deutsche Physikalische Gesellchaft, doi:10.1002/phbl.19480040404

Pollacco D. L., et al., 2006, PASP, 118, 1407

Puschnig J., Posch T., Uttenthaler S., 2014, Journal of Quantitative Spectroscopy and Radiative Transfer, 139, 64–75

Queloz D., et al., 2001, A&A, 379, 279

Rauer H., et al., 2014, Experimental Astronomy, 38, 249

Rhodes B. C., 2011, PyEphem: Astronomical Ephemeris for Python, Astrophysics Source Code Library, record ascl:1112.014 (ascl:1112.014)

Ricker G. R., et al., 2015, Journal of Astronomical Telescopes, Instruments, and Systems, 1, 014003

Sada P. V., et al., 2012, PASP, 124, 212

Salaris M., Cassisi S., 2005, Evolution of Stars and Stellar Populations. John Wiley & Sons

Skrutskie M. F., et al., 2006, AJ, 131, 1163

Smithsonian Astrophysical Observatory 2000, SAOImage DS9: A utility for displaying astronomical images in the X11 window environment, Astrophysics Source Code Library, record ascl:0003.002 (ascl:0003.002)

Taylor M. B., 2005, in Shopbell P., Britton M., Ebert R., eds, Astronomical Society of the Pacific Conference Series Vol. 347, Astronomical Data Analysis Software and Systems XIV. p. 29

Tinetti G., et al., 2012, Experimental Astronomy, 34, 311

Tinetti G., et al., 2018, Experimental Astronomy, 46, 135

Torres G., et al., 2011, ApJ, 727, 24

Tuthill P., et al., 2018, in Creech-Eakman M. J., Tuthill P. G., Mérand A., eds, Society of Photo-Optical Instrumentation Engineers (SPIE) Conference Series Vol. 10701, Optical and Infrared Interferometry and Imaging VI. p. 107011J, doi:10.1117/12.2313269

Udalski A., et al., 1994, Acta Astron., 44, 165

Uttenthaler S., Meingast S., Lebzelter T., Aringer B., Joyce R. R., Hinkle K., Guzman-Ramirez L., Greimel R., 2016, A&A, 585, A145

Virtanen P., et al., 2020, Nature Methods, 17, 261

Walker G., et al., 2003, PASP, 115, 1023

Wang Y.-H., et al., 2019, The Astronomical Journal, 157, 82

West R. G., et al., 2009, A&A, 502, 395

Wheatley P. J., et al., 2018, MNRAS, 475, 4476

Wilson R. E., 1994, PASP, 106, 921

Wolszczan A., Frail D. A., 1992, Nature, 355, 145

Young A. T., 1967, AJ, 72, 747

des Etangs A. L., Lissauer J. J., 2022, New Astronomy Reviews, 94, 101641

van der Walt S., Colbert S. C., Varoquaux G., 2011, Computing in Science and Engineering, 13, 22